Available online at www.sciencedirect.com

ScienceDirect

Underground Space 26 (2026) 1–21

www.keaipublishing.com/undsp

Research Paper

Excavation-induced fracturing mechanisms in deep hard rock: A hierarchical block model

Shili Qiu [a], Shirui Zhang [a,b], Quan Jiang [a,*], Yuheng Fang [a,b], Ping Li [c], Shaojun Li [a], Yaxun Xiao [a], Dingping Xu [a]

[a] State Key Laboratory of Geomechanics and Geotechnical Engineering Safety, Institute of Rock and Soil Mechanics, Chinese Academy of Sciences, Wuhan 430071, China

[b] University of Chinese Academy of Sciences, Beijing 100049, China

[c] South-Central Minzu University, Wuhan 430074, China

Received 14 May 2025; received in revised form 1 July 2025; accepted 3 July 2025
Available online 10 November 2025

Abstract

The fracture characteristics of the excavation damage zones (EDZs) of deeply buried tunnels are closely related to energy evolution, and they are highly valuable for support design. Advanced numerical simulation techniques have shown the potential for evaluating the EDZ properties. On the basis of the finite-discrete element method (FDEM) and Poisson's random block generation technique, the virtual block model (VBM) is proposed to characterize the intact rock masses surrounding tunnels. Moreover, a virtual block upscale principle is proposed to determine the geometric and meso-mechanical parameters. The Canadian Underground Research Laboratory and China Jinping Underground Laboratory Phase II (CJPL-II) project excavations are simulated, and the excavation-induced fracture characteristics of the surrounding rock masses are analyzed in detail. The VBM captures the tensile, shear, and mixed fracture properties under excavation-induced confining pressure evolution. Then, the thicknesses of the spalling rock slabs in Lab #7 of the CJPL-II project are evaluated via the Otsu method. Combined with onsite monitoring data, the validity and advancement of the VBM are verified. This study expands the applicability of the FDEM and provides a new method for assessing the EDZs of surrounding rocks.

Keywords: Strain bursting; Deep tunnel; FDEM; Hard rock; Brittle fracture mechanism

1 Introduction

With the expansion of infrastructure construction into deep underground spaces, deep tunnel engineering has played an increasingly critical role in transportation, water conservancy, and energy fields (Jing & Hudson, 2002). These projects usually face many challenges, such as high ground stresses, complex geological structures, and adverse geological conditions. During tunnel excavation, the original stress balance of the surrounding rock is broken, leading to stress redistribution. Then, an excavation damage zone (EDZ) forms within a certain range around the tunnel. This EDZ severely threatens long-term tunnel stability, support structure design, and operational safety. For example, in the excavation of deeply buried tunnels at the Jinping II hydropower station, the occurrence of a damage zone decreased the rock mass bearing capacity and increased both the support difficulty and project cost. Therefore, in-depth research on the EDZs of deep tunnels and the exploration of more effective prediction and control methods have become urgent issues that must be solved in the deep underground engineering field.

The precise characterization of the EDZ in terms of its spatial extent, morphological features, and evolutionary

* Corresponding author.
E-mail address: qjiang@whrsm.ac.cn (Q. Jiang).
Peer review under the responsibility of Tongji University

https://doi.org/10.1016/j.undsp.2025.07.002

patterns holds significant academic and engineering value for optimizing the design and construction of deep tunnels, ensuring project safety, and minimizing construction costs. Considerable research efforts have been dedicated to this field by scholars worldwide, yielding fruitful achievements in multiple dimensions, including EDZ detection methodologies, formation mechanisms, and numerical modeling approaches. Martin et al. (Martin, 1997; Martin et al., 1999) determined the point where slab failure occurs and proposed an empirical formula for the relationships among the slabbing depth, in-situ stress, and rock strength according to the statistical analysis of slab failure in many underground laboratories constructed in hard rock. Feng et al. (2018a, 2018b) studied the deep displacement and fracturing of hard rock at the CJPL-II site via the photogrammetry method and the digital borehole methods.

Recently, various numerical modeling techniques have been applied to investigate EDZs in the deeply buried tunnels. Numerical back-analysis has shown that the cohesion-weakening-frictional-strengthening model (Diederichs, 2003; Hajiabdolmajid et al., 2002; Perras & Diederichs, 2014; Walton et al., 2014), damage initiation spalling limit (Diederichs, 2007), and progressive S-shaped yield criterion (Sinha & Walton, 2018) can effectively capture the brittle response during excavation. Discrete element methods, such as the discontinuous synthetic rock mass model (Farahmand et al., 2018) and the grain-based model (GBM) based on the phase field method (PF), UDEC, or 3DEC (Dadashzadeh, 2020; Farahmand & Diederichs, 2021; Wang & Cai, 2018) and RBSN (Kim et al., 2017), are used to simulate the evolution of fractures from continuous to discontinuous. The intact rock mass is discretized into Voronoi grains, and the stress-induced fractures of rock masses occur along the boundaries between the Voronoi grains; thus, the intergranular fractures can effectively be observed. However, transgranular fractures also occur during damage evolution; thus, the GBM is important for characterizing transgranular and intergranular fractures. The FDEM-GBM, UDEC-GBM, UDEC-Trigon, PFC-GBM, and PF-GBM methods were developed to simulate the complex fracture evolution (Abdelaziz et al., 2018; Gao et al., 2016; Hu et al., 2020, 2022, 2023; Li et al., 2020). Moreover, a higher-order nonlocal operator method (HONOM) (Ren et al., 2020), a dual-horizon peridynamics (DH-PD) (Ren et al., 2016, 2025), and a novel variational damage model (VDM) (Ren et al., 2024) were developed to simulate elastic materials as well as phase field modeling of fracture.

Although the abovementioned studies have made great progress, these numerical models are mainly used to simulate the laboratory-scale rock fracture process, and the GBM, which is used to characterize the engineering-scale fracture evolution from continuous to discontinuous, needs further study. For example, the engineering-scale UDEC-BBM (Sinha & Walton, 2021) and UDEC-Trigon models (Gao et al., 2019) cannot accurately characterize the confining pressure dependence effect on the pillar fracture mechanism and evaluate expansion deformation. The UDEC-BBM is constructed using polygonal blocks, which can simulate the inelastic deformation inside blocks. Although this model can be used to evaluate bulking, tensile fractures are more easily mobilized because of the presence of unbreakable blocks. The UDEC-Trigon model is constructed using triangular elements; thus, shear fractures are more easily mobilized because these triangular elements have relatively high slip ability. Therefore, scaling the breakable grain size to simulate the mechanical responses of the rock masses is necessary. The fracture mechanisms include tensile splitting under low confining pressure, shear fracture under high confining pressure, and mixed fracture under moderate confining pressure. A robust upscaled GBM must be capable of characterizing intergranular fractures and transgranular fractures. Dadashzadeh (2020) adopted the UDEC-GBM to characterize the EDZs for deep repository engineering and proposed the calibration strategies for the mesoscopic parameters ranging from the laboratory-scale to engineering-scale models.

In this study, based on the FDEM, an upscaling hierarchical grain-based approach is proposed to simulate the fracturing process of the EDZs in intact rock masses and assess the thicknesses of the spalling rock slabs. First, the double-scale breakable virtual block model (dsbVBM) is comprehensively introduced, and the upscaling principles of the breakable block size and meso-parameters are proposed. Then, excavations of the Canadian Underground Research Laboratory (URL) test tunnel and China Jinping Underground Laboratory Phase II (CJPL-II) Lab #7 are simulated. Finally, the simulated failure patterns, depths, and shapes of the EDZs are compared with the field phenomena. Moreover, the thicknesses of the spalling rock slabs in Lab #7 of the CJPL-II project are evaluated.

2 Excavation fracture characteristics (EFCs) at the CJPL-II site

2.1 Engineering background and geological conditions

The tunnels of the CJPL-II site are excavated from intact marble buried at a maximum depth of 2400 m and serve as valuable locations for observing stress-induced EFCs in hard rock masses. The CJPL-II project was established for theoretical physics research on dark matter. The mechanical response of rock masses during the cavern excavation provides valuable insights into rock mechanics studies. The CJPL-II site is located south of the traffic auxiliary tunnel between the chainages AK7+600 and AK8 +150 of the Jinping II hydropower station. This project includes four traffic tunnels and nine laboratory tunnels, as shown in Fig. 1(a)–(c). The CJPL-II laboratory tunnels were excavated via bench excavation (Fig. 1(d)) and completed in September 2015. The entire tunnel group is in an anticline zone with a nearly N-S trending axis. The axis of the traffic tunnel #2 is at the anticline core, and Labs #1–#3 and Labs #4–#8 are in the NW and SE anticline

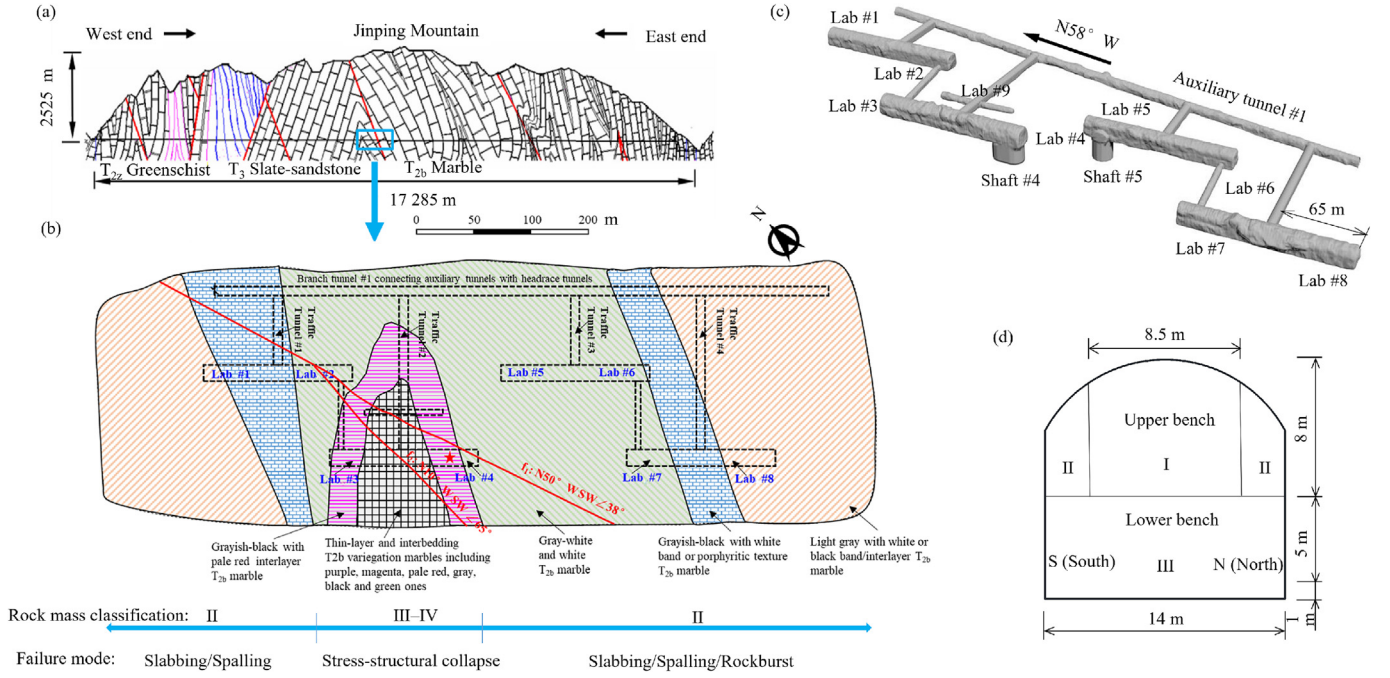

Fig. 1. Construction overview of the CJPL-II project. (a)–(b) Geological setting and rock mass failure mode, (c) CJPL-II tunnel group layout, and (d) excavation sequence and tunnel cross-sectional sizes (Feng et al., 2016).

flanks, respectively. Furthermore, two faults, f_1 and f_2, each with a maximum width of approximately 1 m, can be observed in Labs #2–#4 (Fig. 1(b)). The CJPL-II tunnel group is located in the Triassic strata (Fig. 1(b)).

Moreover, investigations of rock mass integrity and mechanical properties reveal that rock masses are the poorest in the anticline core and the fault-affected areas, whereas they gradually improve toward the two anticline flanks. These flanks are where the rock masses in Labs #7–#8 are already considered relatively massive. Variations in the rock masses and geostress conditions lead to considerable variability in the EFCs during excavation of the CJPL-II tunnel group. As shown in Fig. 1(b), in the anticline core, the rock mass is dominated by stress-structural collapse, whereas in the two anticline flanks, especially in the excavation areas of Labs #7–#8, considerable slabbing, spalling, and rockbursts occur. During the excavation of the CJPL-II tunnel group, in-situ microseism monitoring was conducted to obtain the characteristics of rock mass fracturing and its seismicity. Figure 2(a) shows the spatial distributions of microseism events in the surrounding rock masses with moment magnitudes greater than −2 from April 2015 to September 2015 during the excavation of nine laboratory tunnels. The microseismic events with high moment magnitudes are concentrated and developed in the excavation zones of Labs #7–#8. The in-situ stress was measured via the stress relief method at the west end of Lab #7 (Zhong et al., 2018), which shows that both the maximum and intermediate principal stresses are approximately 70 MPa, and the minimum principal stress is approximately 25 MPa. The directions of the three principal stresses are illustrated in Fig. 2(b). This figure indicates that the excavated sections in Labs #7–#8 are under very high vertical compressive stresses. Moreover, the ratio of the maximum stress to the minimum stress is nearly 2.7, indicating that these sections have extremely anisotropic stress fields.

2.2 Stress-induced EFCs in Labs #7 and #8

The EFCs of tunnels mainly appear in Labs #7 and #8 due to the geostress, rock mass structure, tunnel shape, and excavation sequence. Five tunnel intervals in Labs #7 and #8 (Zones I to V shown in Fig. 2(b)) are selected to identify the stress-induced fracturing characteristics of the surrounding rock masses and their major controlling factors.

As shown in Fig. 3(a), in Zone I (K0−45 to K0−50 in Lab #8), considerable spalling failures can be observed on the south sidewall and shoulder and the north footwall of the middle pilot tunnel. The failed rock masses include many rock slabs with thicknesses of 2–15 cm that are parallel to the sidewall boundaries. Rock slabs are mechanically formed with stress-induced tensile fractures. The arrows in the center of the pink dotted lines represent the opening directions of the extension fractures. Moreover, the red dotted lines also represent shear fractures, and they are indicative of the overstrained shear rupture mechanisms of rock slabs with bulking behaviors.

Following the excavation of the middle pilot tunnel in Zone I rock masses and after the excavation blasting of the lower bench of Lab #7 from the strike K0+25 to K0 +31, an extremely strong rockburst (8.23 rockburst) occurred at the southern sidewall between the strikes K0

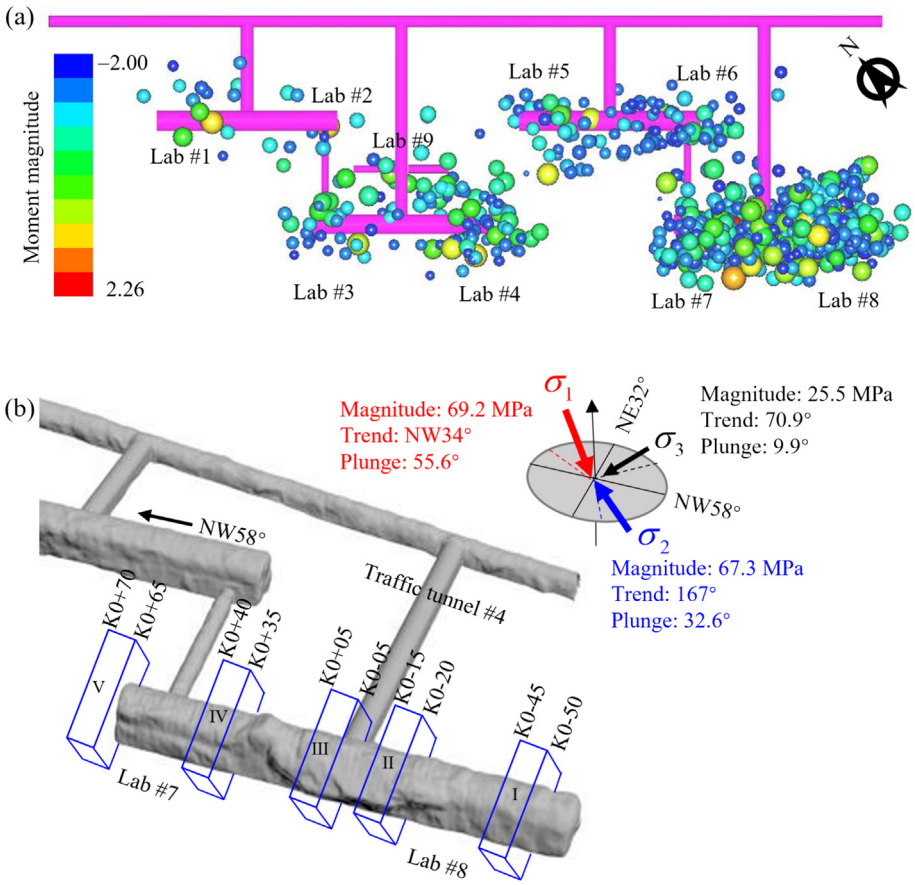

Fig. 2. Fracturing behaviors of rock masses of the CJPL-II site. (a) Spatial distributions of microseismic events with moment magnitudes greater than −2 from April 2015 to September 2015, and (b) in-situ stress conditions in the regions of Labs #7 and #8 and five typical tunnel intervals for EFC identification.

−35 in Lab #8 and K0+09 in Lab #7. This rockburst resulted in 350 m^3 of ejected rock mass, forming a damage zone of approximately 44 m in length, 6 m in height, and 3.2 m in depth (Fig. 3(b)). In this rockburst case, a primary seismic source zone can be identified in the southern sidewall rock masses from the strike K0−17 in Lab #8 to K0 +07 in Lab #7, in which the mixed fracture process occurred on a closed and ferromanganese-cemented structure plane with an attitude of N65°W SW∠65°, as shown in the magnified photo on the right of Fig. 3(b)–(c). The mixed fracturing process was induced by the unloading of the surrounding pressure due to the excavation of the lower bench in Lab #7. The strong vibrations evoked by the dynamic fracturing process, which had a local magnitude of 1.0 according to the waveform analysis of microseismic system monitoring, led to a severe structure-controlled collapse of the rock masses that are composed of stress-induced fractures and sparse joint sets, e.g., a joint set with an orientation of N60°E NW∠15°, as shown in the magnified photo on the left of Fig. 3(b). A rupture of the structural surface striking along the axial direction of the tunnel constituted the main seismic source of this rockburst event.

3 Virtual block model based on the FDEM

3.1 Main principles of the FDEM

The FDEM (Munjiza et al., 1995) was initially proposed to simulate the behaviors of multiple deformable bodies and their dynamic interactions, and then further developed to simulate rock behavior by explicitly modeling rock elastic deformation, crack initiation, and crack propagation. This method can detect new contact sites and consider the translation, rotation, and interaction of discrete bodies. In this study, IRAZU^{2D} software (Geomechanica Inc., 2021) is used to implement the proposed hierarchical grain-based approach.

3.1.1 Governing equation

In the 2D FDEM, the rock material is discretized with elastic triangular element (ETE) pairs bonded via zero-thickness 4-noded cohesive crack elements (CCEs). The ETEs are used to capture the elastic mechanical response, and the CCEs are used to capture crack initiation and growth. The generalized governing equation of motion in the FDEM can be expressed as follows (Munjiza et al., 1995):

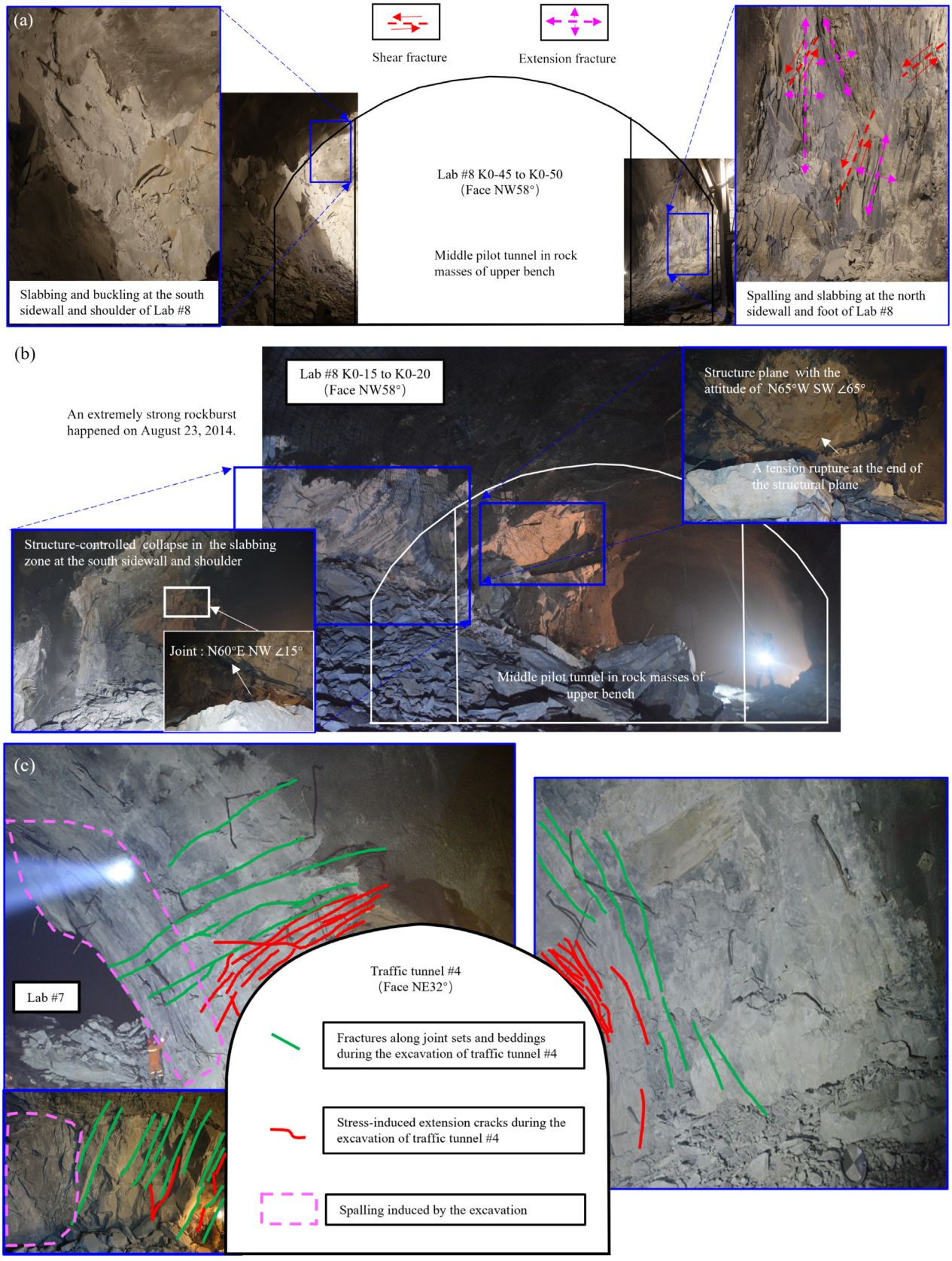

Fig. 3. Stress-induced fracturing characteristics of tunnel intervals in Labs #7 and #8. (a) Spalling in Lab #8, (b) rockburst in Lab #8, and (c) spalling in Lab #7.

$$\boldsymbol{M}\frac{\partial^2 \boldsymbol{x}}{\partial t^2}+\boldsymbol{C}\frac{\partial \boldsymbol{x}}{\partial t}+\boldsymbol{f}_{\mathrm{int}}(\boldsymbol{x})-\boldsymbol{f}_{\mathrm{ext}}(\boldsymbol{x})-\boldsymbol{f}_{\mathrm{c}}(\boldsymbol{x})=0, \tag{1}$$

where $\boldsymbol{M}$ is the system mass matrix; $\boldsymbol{C}$ is the viscous damping matrix; $\boldsymbol{x}$ is the vector of nodal displacements; $\boldsymbol{f}_{\mathrm{int}}$ is the vector of internal resisting forces, which is mainly composed of elastic reaction forces ($\boldsymbol{f}_{\mathrm{e}}$) and crack element bonding forces ($\boldsymbol{f}_{\mathrm{b}}$); $\boldsymbol{f}_{\mathrm{ext}}$ is the vector of applied external loads; and $\boldsymbol{f}_{\mathrm{c}}$ is the vector of contact forces. The role of each parameter in Eq. (1) in the main calculation loops is shown in Fig. 4.

3.1.2 Contact interaction of ETEs

In the FDEM, many contact identifications and contact force calculations of ETEs must be performed. The contact calculation involves two algorithms, namely, the contact detection algorithm (CDA) and the contact interaction algorithm (CIA) (Lisjak et al., 2018). CDA is aimed at detecting potential contact pairs of ETEs. CDA is implemented via a two-step approach. First, the modeling domain is divided into square grids to obtain the grid coordinates of each mapped ETE, and any two ETEs mapped to the same grid cell represent a potential contiguous pair. Then, the contact intersection testing is performed by projecting the potential contiguous ETEs onto a separating axis and checking for overlap of the intervals containing ETE projections. If two ETEs overlap, ETE contact occurs. Thus, the interaction forces between two contiguous ETEs need to be calculated via the CIA. In the CIA, two types of forces (repulsive and frictional forces) are applied to contiguous ETEs. The repulsive forces are computed via a distributed contact force penalty function (Munjiza & Andrews, 2000). Contiguous ETEs tend to penetrate each other, generating distributed contact forces that depend on the shape and size of the overlap between the two ETEs and the value of the penalty term. The repulsive forces can be formulated via Eq. (2), where E_{t} and E_{c} are the target and contactor of each pair of contacting finite elements, respectively, $\varphi_{\mathrm{t}}(P_{\mathrm{t}})$ and $\varphi_{\mathrm{c}}(P_{\mathrm{c}})$ are the potential functions of the target and contactor at the contact points P_{t} and P_{c}, respectively, and $S=E_{\mathrm{t}}\cap E_{\mathrm{c}}$ is the overlapping area of two contiguous ETEs:

$$\boldsymbol{f}_{\mathrm{c}}=\int_{S=E_{\mathrm{t}}\cap E_{\mathrm{c}}}\mathrm{grad}\varphi_{\mathrm{c}}(P_{\mathrm{c}})-\mathrm{grad}\varphi_{\mathrm{t}}(P_{\mathrm{t}})\mathrm{d}A. \tag{2}$$

The potential (P_{c}) at each contact point of a TE is given by Eq. (3), where p_{n} is the normal penalty coefficient; A is the elemental area; A_1, A_2, and A_3 are the areas of the

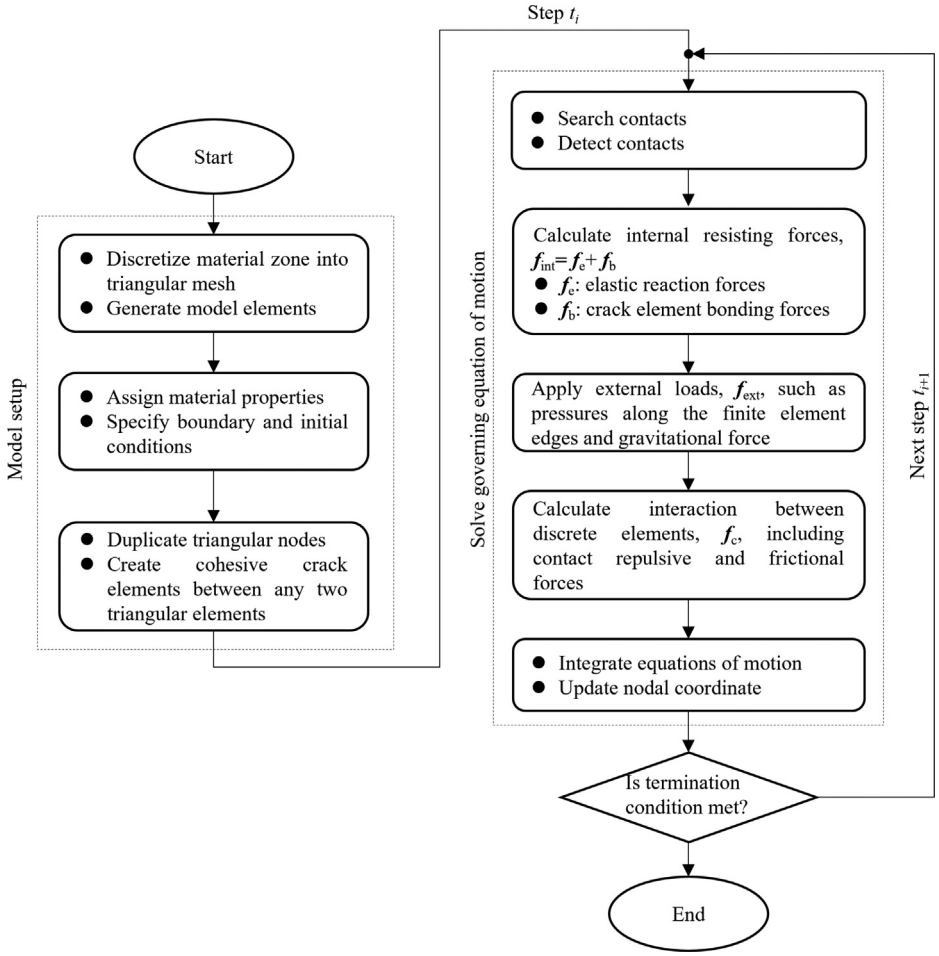

Fig. 4. Flowchart of the main loops in the 2D FDEM simulation.

triangles formed by connecting three nodes of the ETE to the point P_c. The potential is equal to p_n at the centroid of the triangular element when $A_1 = A_2 = A_3$ and is equal to zero along the ETE edges. The gray area in Fig. 5 represents the distribution of the potential on AB and defines the total contact force exerted on the edge AB of $E_{contactor}$ due to the potential of the triangle E_{target}. This force is applied as equivalent nodal forces at points A and B and as reactionary forces in the opposing direction on the nodes of E_{target}.

$$\varphi_c(P_c) = \begin{cases} p_n \cdot \min\{3A_1/A,\ 3A_2/A,\ 3A_3/A\}, & \text{if } P_c \text{ is inside the element } E_c \\ 0, & \text{Otherwise} \end{cases} \tag{3}$$

Moreover, the frictional force of each contact pair is used to simulate the shear strengths of intact material and pre-existing and newly generated fractures. The frictional force vectors are calculated via a Coulomb-type friction law. The frictional resistance is mobilized over a finite amount of relative displacement between the interacting edges, which is denoted as the sliding distance (δ_s). Hence, the tangential stress (σ_t) is calculated via Eq. (4):

$$|\sigma_t| = \min\{p_t \cdot h \cdot |\delta_s|,\ |\mu \cdot \sigma_n|\}, \tag{4}$$

where h is the element edge length; p_t is the tangential penalty coefficient; σ_n is the normal stress across the interacting edges; μ is the user-specified friction coefficient, which can be calculated via $\mu = \tan\phi_f$; ϕ_f is the internal friction angle of the contact edges.

3.1.3 Cohesive crack elements for rock fracturing simulations

The rock fracturing process is simulated via an intrinsic fracture process zone (FPZ) (Fig. 6(a) and (b)). The modeling domain is discretized with ETE pairs bonded via CCEs (Fig. 6(c)). The tensile and shear softening of a CCE are applied as a function of the crack opening displacement (o) and shear displacement (s), respectively. The CCEs may yield under mode I (Fig. 6(d)), mode II (Fig. 6(e)), or mode I–II (Fig. 6(f)) conditions.

Under tensile loading, the response of each crack element depends on the tensile strength (f_t) and the Mode I fracture energy (G_I). At the peak point, the opening of a CCE reaches a critical value (o_p) corresponding to f_t. After the peak point, a softening law (Eq. (5)) controls the gradual decrease in normal stress from the f_t until the opening of a CCE exceeds the residual opening value (o_r). $f(D)$ is a softening function (Evans & Marathe, 1968):

$$\sigma_n = f_t \cdot f(D),\ 0 \le D \le 1, \tag{5}$$

where D is a damage coefficient with a value between 0 and 1. The residual opening o_r depends on the energy release rate of Mode I fracture, given by Eq. (6):

$$G_I = \int_{o_p}^{o_r} \sigma_n(o)\mathrm{d}o. \tag{6}$$

Similarly, under shear loading, the shear stress of Mode II fracture is calculated via a slip-weakening law (Eq. (7)). The residual shear slippage (s_r) depends on the Mode II fracture energy, given by Eq. (8), where s_p is the critical value of the tangential slip of a CCE, corresponding to the intrinsic shear strength of the element, $f_s = c + \sigma_n \cdot \tan\phi_i$, c is the internal cohesion, and ϕ_i is the intact material friction angle of the CCE. Moreover, $f_r = \sigma_n \cdot \tan\phi_f$ is the residual shear strength, and ϕ_f is the friction angle.

$$\tau = f_s \cdot f(D) \tag{7}$$

$$G_{II} = \int_{s_p}^{s_r} [\tau(s) - f_r]\mathrm{d}s \tag{8}$$

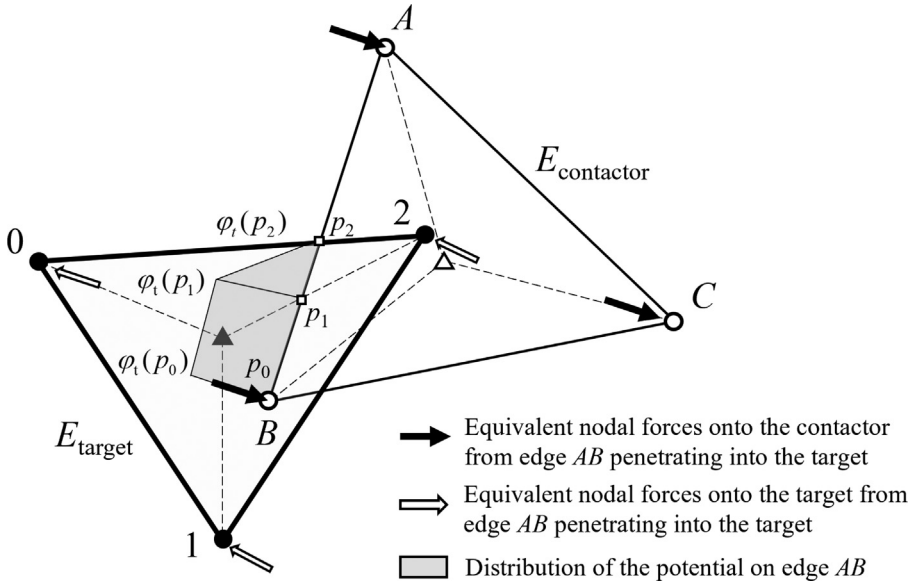

Fig. 5. Illustrations of contact interaction calculations from a distributed contact force penalty function in the FDEM (Tatone & Grasselli, 2015).

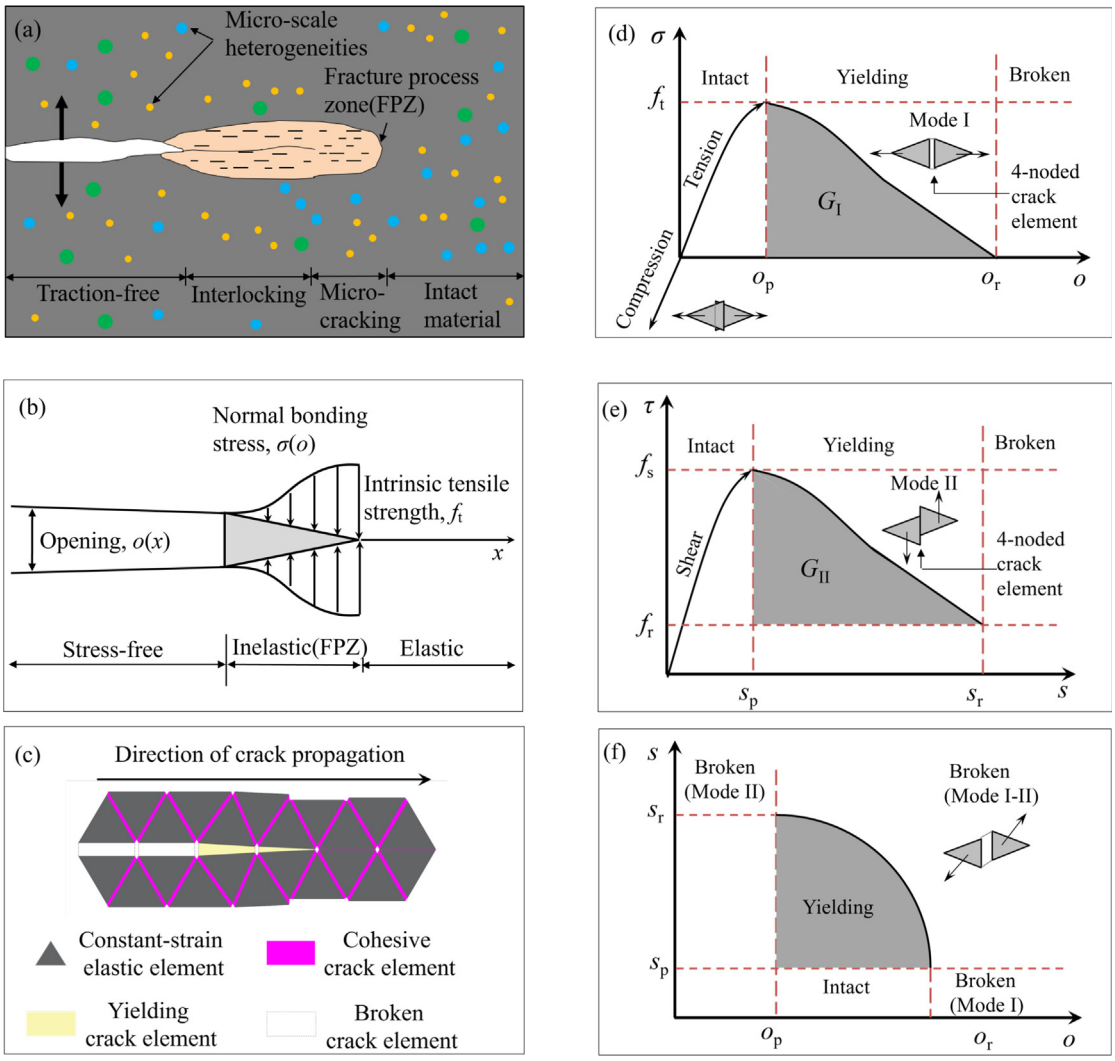

Fig. 6. Conceptual models and mechanical behaviors of cohesive crack elements in the FDEM (Zhang et al., 2024a). (a) Schematic of the fracture process zone (FPZ) in brittle materials, (b) theoretical FPZ model, (c) numerical representation of the theoretical FPZ model, (d) cohesive model for Mode I, (e) slip-weakening model for Mode II, and (f) criterion for mixed-mode fracture initiation.

3.2 Double-scale breakable virtual block model

To capture the stress-induced fracturing process of the hard surrounding rock, a dsbVBM based on the FDEM is proposed. The model splits the intact rock mass around the tunnel into blocks with CCEs at their boundaries (Fig. 7(a)). The blocks are generated via the Voronoi tessellation approach. These blocks are deformable and breakable, and can provide the potential fracture paths, such as splitting and shear slip. The virtual blocks are discretized into triangular blocks via inserted intra-block CCEs (Fig. 7(b)). The intra-CCEs make virtual blocks breakable to characterize the grain-scale transgranular fracturing. Moreover, the inter-CCEs and intra-CCEs can be assigned two different mechanical properties, which can be used to characterize the tensile, shear, and mixed fracture mechanisms of large rock masses around underground openings. The dsbVBM clearly differs from the breakable grain-based model (Gao et al., 2016). The virtual blocks and CCEs in the dsbVBM constitute an artificial energy dissipation structure and do not represent the actual rock mass structure. To some extent, these artificial objects may characterize the randomly distributed mesoscopic defects in hard rock masses. Moreover, a critical upscaling strategy for the dsbVBM is suggested to determine the mechanical parameters of two CCEs for simulating the fracturing of the hard surrounding rock, which differs from the simulation of the micromechanical behaviors of low-porosity or crystalline rocks. In Section 3.3, an upscaling approach for parameter determination of the dsbVBM is explained in detail.

In the dsbVBM, Voronoi tessellation is used to generate a mesh structure of the first-scale virtual blocks. Voronoi tessellation has been extensively adopted to represent polycrystalline rocks at the grain scale (Hu et al., 2020; Peng et al., 2018; Zhang et al., 2024b). The 2D Voronoi tessellation is a cell collection without overlaps or gaps. These cells are convex polygons and are formally defined

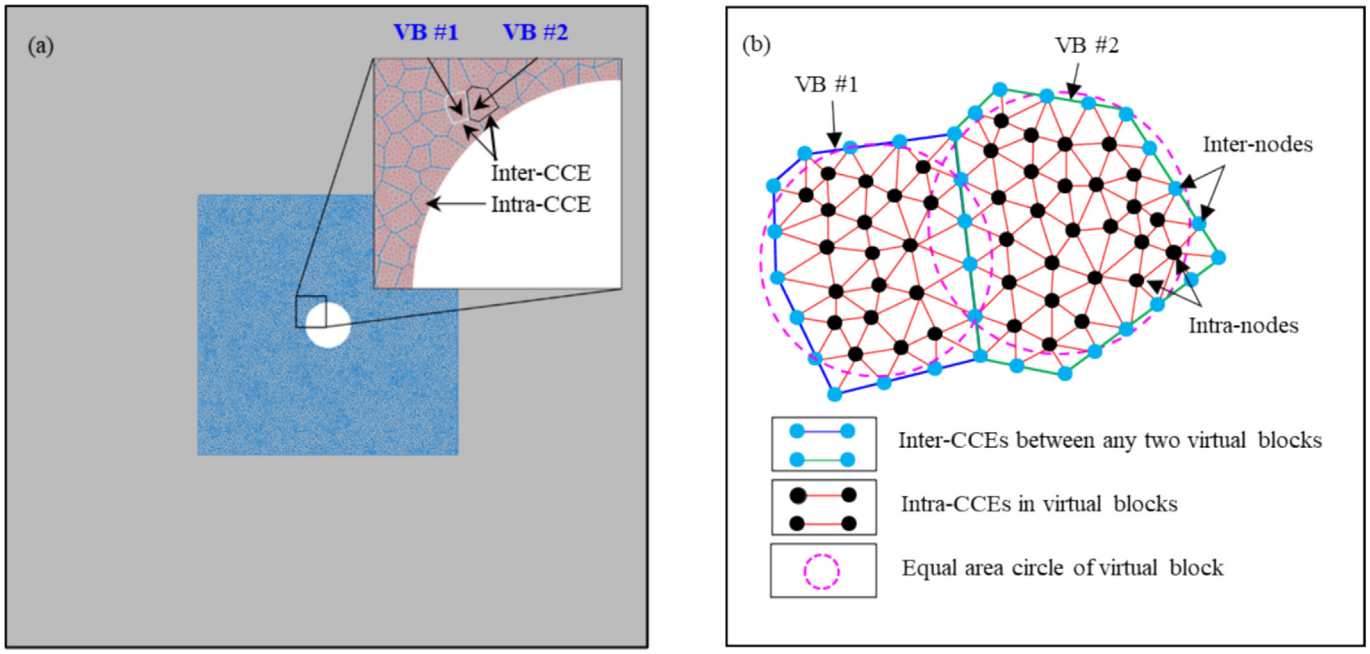

Fig. 7. Schematic chart of the dsbVBM. (a) Large rock masses discretized by virtual Voronoi blocks and inter-CCEs, and (b) virtual blocks divided into triangular blocks by the intra-CCEs.

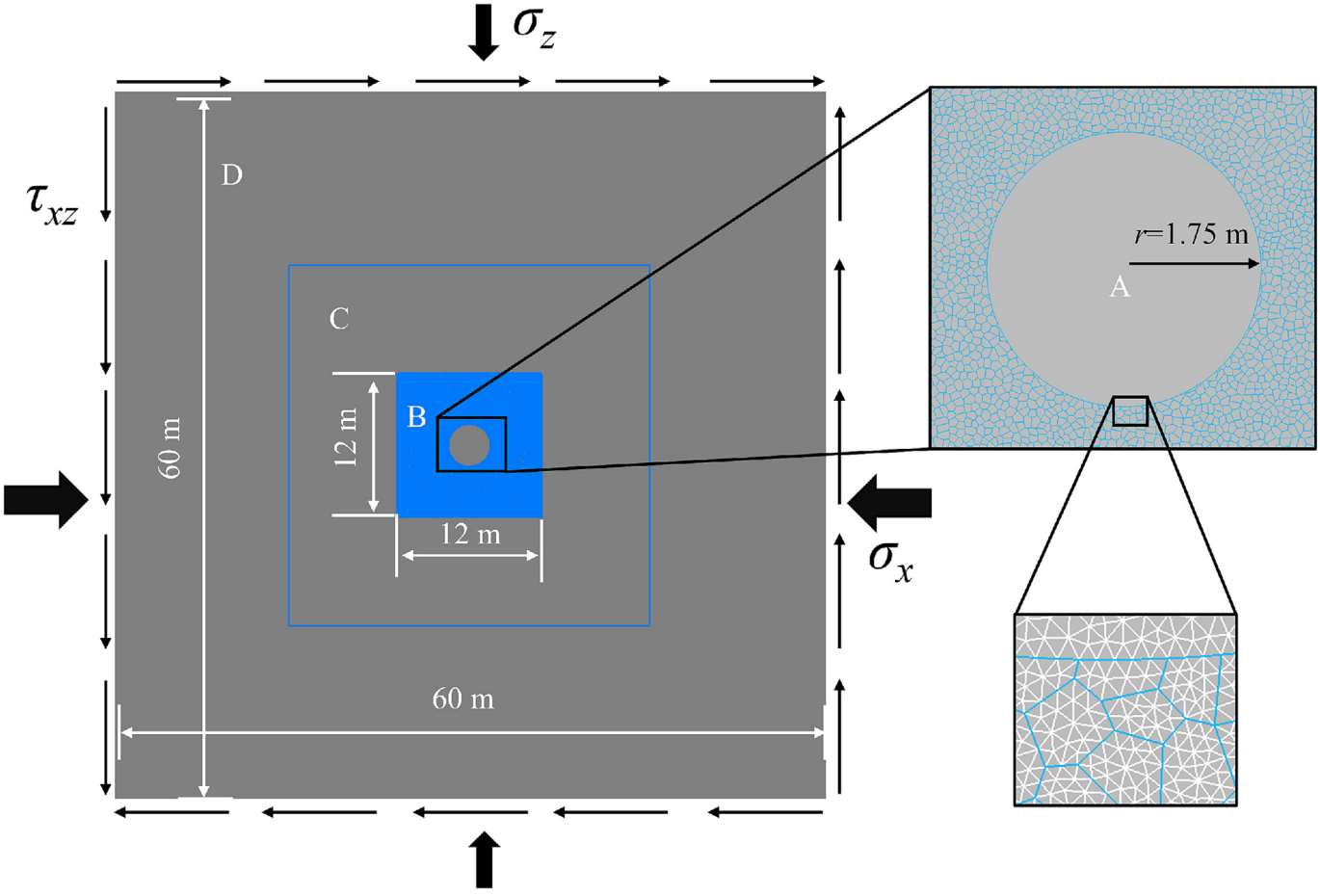

Fig. 8. Model configuration of the URL test tunnel. The different sub-domains depending on the assigned element size are A (0.5–0.03 m), B (0.03 m), C (0.03–1.5 m), and D (1.5–2.5 m).

as influence zones of a randomly distributed set $\boldsymbol{E} = \{G_i(\boldsymbol{x}_i)\}$ of points within a spatial domain ($L \in \Re^2$) corresponding to their centers. Each point in $\boldsymbol{E}$ has a convex polygon region that is closer to that point than to any other point in $\boldsymbol{E}$. The convex polygon region is called a Voronoi cell (C_i), which can be mathematically denoted as (Quey et al., 2011):

$$C_i = \left\{P(\boldsymbol{x}) \in L | l(P, G_i) < l(P, G_j) \quad \forall i \neq j\right\}, \tag{9}$$

where $l(P, G_i)$ is the Euclidean distance.

In this study, Neper (Quey et al., 2011) is used to generate the Voronoi blocks. The Voronoi diagram is controlled by specifying custom cell properties such as sizes, sphericities, and centroids. Moreover, the regularization technique is utilized to remove small Voronoi cell edges to minimize the local geometric distortions, improve computational efficiency, and reduce difficulty in meshing second-scale triangular elements. The Voronoi diagram generated by Neper is subsequently translated into the Gmsh (Geuzaine & Remacle, 2009) via a C++ subroutine. In Gmsh, each Voronoi cell is meshed into an assembly of triangular elements whose lengths are below a given threshold limit. The dsbVBM is imported into IRAZU software (Lisjak et al., 2018) in which the first-scale CCEs are assigned to bond Voronoi blocks, and the second-scale CCEs are assigned to bond triangular blocks.

3.3 Upscaling technique of the FDEM-dsbVBM

3.3.1 Geometric upscaling approach for the virtual block

To apply the dsbVBM for simulating the fracturing behaviors of the field rock masses around tunnels, a Voronoi tessellation with some grains or a specific block size must be meshed and cover the entire simulation domain. The size (radius of the equivalent area circle) of the virtual block is a vital geometrical parameter to limit the Voronoi structure formed from the first-scale CCEs (Fig. 7(b)). The maximum size is set to 4–5 times the average thickness of the field rock slabs. When field-measured data are lacking, a suggested semi-empirical method is proposed (Qiu et al., 2014) (Eq. (10)):

$$t = \left(\frac{K_{\mathrm{Ic}}}{\sqrt{5} \cdot k_{\mathrm{s}}}\right)^{2/3} \text{ or } \left(\frac{0.1453 \cdot T}{\sqrt{5} \cdot k_{\mathrm{s}}}\right)^{2/3}, \tag{10}$$

where k_{s} (GPa/m) is the shear stiffness of the splitting surface, K_{Ic} is the mode I fracture toughness, and T is the uniaxial tensile strength. Qiu et al. (2014) provided an empirical estimator that draws on the Barton-Bandis shear strength criterion of the joint and shear displacement limit (δ_{p}):

$$k_{\mathrm{s}} = \tau_{\mathrm{p}} / \delta_{\mathrm{p}}, \tag{11}$$

where δ_{p} and τ_{p} are calculated via Eqs. (12) and (13), respectively.

$$\delta_{\mathrm{p}} = 0.0077 \cdot L^{0.45} \left(\frac{\sigma_{\mathrm{n}}}{\sigma_{\mathrm{J}}}\right)^{0.34} \cdot \cos\left(\mu_{\mathrm{J}} \cdot \lg\left(\frac{\sigma_{\mathrm{J}}}{\sigma_{\mathrm{n}}}\right)\right), \tag{12}$$

$$\tau_{\mathrm{p}} = \sigma_{\mathrm{n}} \left(\mu_{\mathrm{J}} \cdot \lg\left(\frac{\sigma_{\mathrm{J}}}{\sigma_{\mathrm{n}}}\right) + \phi_{\mathrm{r}}\right), \tag{13}$$

where σ_{n} is the normal stress across the fracture surface, which is 0.1 MPa for the no support condition and 1 or 2 MPa for the high support pressure condition, ϕ_{r} is the residual friction angle, which is suggested to be 30° for splitting surfaces, σ_{J} is the joint roughness coefficient, which is suggested to be 6–8 for a fresh splitting surface, μ_{J} is the joint compressive strength, which is usually valued as the uniaxial compressive strength of the rock, and L (m) is the length of the rock slab determined from the width-height ratio of the slabbing region.

3.3.2 Upscaling approach for determining the mechanical parameters of the virtual block

The triangular element size is closely related to the project scale. For high-efficiency numerical simulations, a hypothesis is suggested to ensure mesh compatibility. The block size is at least twice that of the triangular element. The meso-properties of inter-CEEs and ETEs are determined according to laboratory mechanics parameters; those of intra-CEEs increase correspondingly on the basis of those of inter-CEEs. The calibration suggestions for modeling technology, which are based on laboratory data, field investigations, and empirical formulas, are shown in Table 1.

4 Simulation of the fracture behavior of surrounding rock during excavation

4.1 Model set-up

4.1.1 Geometry and mesh configuration

The Canadian URL test tunnel model comprises three parts: a circular tunnel domain, a near-field surrounding rock constructed by virtual blocks, and a far-field rock mass. The tunnel radius is 1.75 m, and the near-field surrounding rock is a 12 m × 12 m rectangle (see Fig. 8). To eliminate the influence of tunnel excavation on the far-field boundary, the model domain is a 60 m × 60 m rectangle. The grid refinement zone is domain B. The grid refinement zone eliminates the effects of the element size on the crack propagation paths. The element size surrounding the tunnel is 0.03 m, and the outermost element size is 2.5 m. The run parameters are shown in Table 2.

The model of the CJPL-II Lab #7 site comprises a D-shaped tunnel and surrounding rock. The near-field surrounding rock is a 40 m × 24 m rectangle, and the model domain is a 200 m × 200 m rectangle. The mesh refinement zone is a 40 m × 24 m rectangle surrounding the tunnel (domain B in Fig. 9). The element size around the tunnel is 0.09 m, and the outermost element size is 4 m. The run parameters are shown in Table 2.

Table 1
Upscaling algorithm for determining the mechanical parameters of dsbVBM.

Step 1: Determine the grain sizes of rock specimens (e.g., equivalent circle diameter) $d \Leftarrow d \in [4,5]t$, where t is the average thickness of a rock slabs that may occur in the engineering field $\Leftarrow$ initialize t via on-site investigations or a theoretical assessment introduced in Eq. (12).
Step 2: Continuum parameters $\Leftarrow$ initialize ρ, E and v from laboratory tests (i.e., uniaxial compressive tests).
Step 3: Penalty parameters: p_{f}, p_{n} and p_{t} $\Leftarrow p_i \in [1,10]E$, where $i = \mathrm{f},\ \mathrm{n},\ \mathrm{t}$.
Step 4: Determine the trial scale factor λ_i with $i = f,n,t \Leftarrow$ Trial for the penalty parameters of the grain
Loop for λ_i in the trial list $\lambda_i \in [1,10]$ with equal space **do**
//uniaxial compression test calibration
If $\left|\frac{E_{\mathrm{trial}}-E_{\mathrm{test}}}{E_{\mathrm{test}}}\right| << \zeta$ and $\left|\frac{v_{\mathrm{trial}}-v_{\mathrm{test}}}{v_{\mathrm{test}}}\right| << \zeta$ // target continuum parameters E_{test}, v_{test}. ζ is a loop termination condition, i.e., $\zeta = 0.05$;
then
Scale λ_i is defined;
exit loop
else
$\lambda_i \rightarrow \lambda_i^{\mathrm{next}}$;
end if
end loop
Step 5: Strength parameters for inter-CCEs $\Leftarrow c$ and μ, which are consistent with the laboratory data; $f_{\mathrm{t}}^{\mathrm{trial}} = \alpha \cdot f_{\mathrm{t}}^{\mathrm{test}}$, where $f_{\mathrm{t}}^{\mathrm{test}}$ is tension strength obtained from Brazil splitting tests.
Step 6: Strength parameters for intra-CCEs $\Leftarrow$ scale up on strength parameters of virtual inter-block joint $x_{\text{intra - CCE}} = \beta \cdot x_{\text{inter - CCE}}$, where x is c, μ, f_{t}.
Step 7: α, $\beta \Leftarrow$ Trial for the tensile strength of virtual inter-block joints
Loop for α in the trial list $\alpha \in [0.1, 0.2]$ and β in the trial list $\beta \in [1.5, 2.0]$ **do**
//Brazilian disc test calibration
If $\left|\frac{f_{\mathrm{t}}^{\mathrm{trial}}-f_{\mathrm{t}}^{\mathrm{test}}}{f_{\mathrm{t}}^{\mathrm{test}}}\right| << \zeta$ // target tension strength of the rock, $f_{\mathrm{t}}^{\mathrm{test}}$
then
scale α and β are defined;
exit loop
else
$\alpha \rightarrow \alpha_{\mathrm{next}}$
$\beta \rightarrow \beta_{\mathrm{next}}$
end if
end loop
Step 8: G_{I} and G_{II} of inter-CCEs $\Leftarrow$ theoretical values, $G_{\mathrm{I}} = \frac{(1-v^2)f_{\mathrm{t}}^2}{47.33E}$, $G_{\mathrm{II}} = 10G_{\mathrm{I}}$
Step 9: G_{I} and G_{II} of intra-CCEs $\Leftarrow$ scale up on G_{I} and G_{II} of inter-CCEs $y_{\text{intra - CCE}} = \eta \cdot y_{\text{inter - CCE}}$, where y is G_{I} and G_{II}.
Step 10: $\eta \Leftarrow$ Trial for G_{I} and G_{II} of intra-CCEs
Loop for η in the trial list $\eta \in [1.3, 1.5]$ **do**
//uniaxial compression test calibration
If $\left|\frac{\sigma_{\mathrm{trial}}-\sigma_{\mathrm{test}}}{\sigma_{\mathrm{test}}}\right| << \zeta$ // target uniaxial compressive strength σ_{test}
then
scale η is defined;
exit loop
else
$\eta \rightarrow \eta_{\mathrm{next}}$
end if
end loop
Step 11: Determine the upscaling size of the virtual block (equivalent circle diameter) $d \Leftarrow d \in [4,5]t$, where t is the average thickness of a rock slab that may occur in the engineering field $\Leftarrow$ initialize t via on-site investigations or a theoretical assessment introduced in **Eq.** (12).
Step 12: Based on the input parameters determined by the above process, the initial simulation is performed, and the ground stress conditions are determined according to the measured data.
do
// excavation simulation test verification
If $\left|\frac{D_{\mathrm{trial}}^{\mathrm{EDZ}}-D_{\mathrm{measured}}^{\mathrm{EDZ}}}{D_{\mathrm{measured}}^{\mathrm{EDZ}}}\right| << \zeta$
then
upscaling model of the defined parameters;
else
adjust the parameters of the upscaling model;
end if
Step 13: Adjustment of the strength parameters for upscaling model, including c, μ, G_{I} and $G_{\mathrm{II}} \Leftarrow$ Trial for the inter-CCE parameters. Note that no change occurs for intra-CCE parameters
do
// uniaxial compression test calibration and excavation simulation
if $\left|\frac{D_{\mathrm{trial}}^{\mathrm{EDZ}}-D_{\mathrm{measured}}^{\mathrm{EDZ}}}{D_{\mathrm{measured}}^{\mathrm{EDZ}}}\right| << \zeta$ and $\left|\frac{\sigma_{\mathrm{trial}}-\sigma_{\mathrm{test}}}{\sigma_{\mathrm{test}}}\right| << \psi$ // target damage zone extent $D_{\mathrm{measured}}^{\mathrm{EDZ}}$. ψ is a loop termination condition, i.e., $\psi = 0.3$;
then
upscaling model of the defined parameters;
end if

Table 2
Run parameters for the conducted analyses.

Project	Model type	Time step size (s)	Time step	Element size (m)*	Number of elements
URL	FDEM	6.1×10^{-8}	1 400 000	0.03	674 407
	FDEM-VBM	2.5×10^{-8}	1 700 000	0.03	658 724
CJPL-II	FDEM	1.5×10^{-7}	1 500 000	0.09	401 984
	FDEM-VBM	4.0×10^{-8}	1 900 000	0.09	525 804

Note: * Average element size assigned to the elements in the high-resolution domain B.

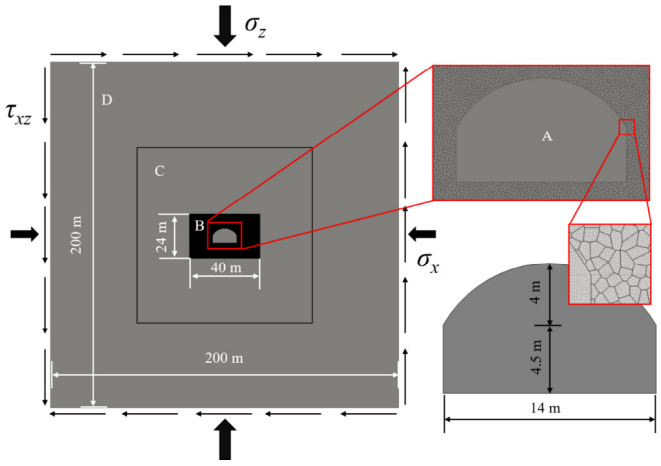

Fig. 9. Model configuration of the CJPL-II Lab #7 site. The different sub-domains depending on the assigned element size are A (0.5–0.09 m), B (0.09 m), C (0.09–2.0 m), and D (2.0–4.0 m).

4.1.2 Simulation process

The model is divided into two sub-domains, in which Voronoi blocks are distributed only near the tunnel to evaluate the fracture process during the excavation. With respect to the excavation sequence employed in the numerical model, a uniform stress field is initially applied in the model domain. Static equilibrium at the end of the geostatic stress stage is guaranteed by ensuring that the displacement is initialized to zero and that the assigned stress is equal to the measured stress in the model. The geostatic stress stage is followed by tunnel excavation. The face replacement method (Curran et al., 2003) is used to simulate the 3D effect of the tunnel face advancement. This goal is achieved by decreasing the Young's modulus of the rock material within the excavation boundary (Vlachopoulos & Diederichs, 2014). Finally, the excavated material is completely removed. For each stage, adequate time steps are performed to ensure the static conditions and mitigate the dynamic effect induced by excavation. The isotropic model is used. A maximum of 1 900 000 steps was performed for the modelling sequence in this study with a maximum runtime of approximately 48 h on an Intel® Xeon® W-2123 CPU at 3.60 GHz, 64 GB RAM, and an NVIDIA Quadro RTX 6000 GPU.

4.2 Input parameters

The measured geostresses in the URL test tunnel and the CJPL-II laboratory are shown in Table 3. For the traditional FDEM model, which is based on the rock mechanical parameters obtained from the laboratory tests, a trial-and-error method is used to calibrate the meso-parameters. For the dsbVBM, the upscaling approach proposed in Section 3.3 is used to determine the meso-parameters (see Tables 4 and 5).

5 Numerical results and FDEM-VBM verification

5.1 Comparison verification of the Canadian URL test tunnel

The Canadian URL test tunnel in southeastern Manitoba, Canada, is a complex of test chambers excavated in granite by Atomic Energy of Canada Limited to study the long-term safety of underground nuclear waste disposal, and it is located at the 420 m level (Fig. 10(a) and (b)). During excavation of the URL test tunnel, a multi-

Table 3
Geostress boundary conditions (Martin, 1997; Zhong et al., 2018).

Stress component	URL	CJPL-II
σ_{xx} (MPa)	−58.00	−60.81
σ_{zz} (MPa)	−13.00	−66.89
τ_{xz} (MPa)	−9.20	−19.00

Table 4
Input parameters for the traditional FDEM simulation.

Parameter	URL	CJPL-II
Density (kg/m^3)	2600	2750
Young's modulus (GPa)	65	60
Poisson's ratio	0.18	0.25
Viscous damping factor	1	1
Fracture penalty (GPa)	650	600
Normal contact penalty (GPa)	650	600
Tangential contact penalty (GPa)	650	600
Friction coefficient	1.7	1.1
Cohesion (MPa)	50	50
Tensile strength (MPa)	10	5
Mode I fracture energy (N/m)	300	300
Mode II fracture energy (N/m)	1900	3000

Table 5
Input parameters for the FDEM-VBM simulation.

Model type	Properties	Parameters	URL	CJPL-II
ETE	Deformation	Density (kg/m^3)	2600	2750
		Young's modulus (GPa)	65	60
		Poisson's ratio	0.18	0.25
		Viscous damping factor	1	1
		Fracture penalty (GPa)	650	600
		Normal contact penalty (GPa)	650	600
		Tangential contact penalty (GPa)	650	600
Intra-CCE	Strength	Friction coefficient	2.2	1.7
		Cohesion (MPa)	80	100
		Tensile strength (MPa)	16	10
		Mode I fracture energy (N/m)	300	400
		Mode II fracture energy (N/m)	3000	4000
Inter-CCE	Strength	Friction coefficient	1.7	1.1
		Cohesion (MPa)	50	55
		Tensile strength (MPa)	2	1
		Mode I fracture energy (N/m)	200	300
		Mode II fracture energy (N/m)	2000	3000

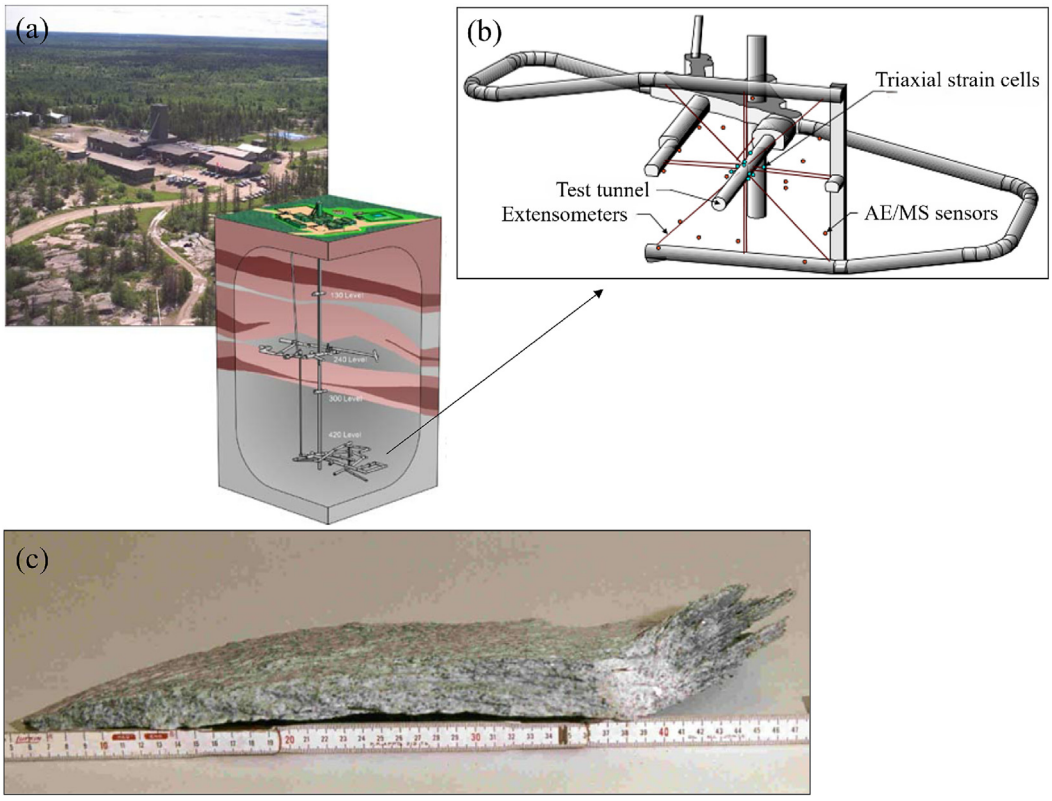

Fig. 10. Overview of the URL. (a) URL surface facilities (photograph), and generalized geology of the Lac du Bonnet batholith near underground developments (schematic drawing), (b) layout of the mine-by experiment at the 420 level of the URL, and (c) typical rock slab detached from the URL test tunnel during the progressive failure process. (Read, 2004; reproduced with permission, courtesy of Elsevier).

stage process of progressive brittle failure was observed. The process resulted in the development of two V-shaped notches (Fig. 11(a)), which are typical of borehole breakouts under high-stress conditions. These notches developed in areas where compressive stress was concentrated in the tunnel crown and invert. Breakouts were more evident and developed more readily in areas with granite than in areas with granodiorite lithologies. The breakout notches were found to be in a state of meta-stable equilibrium, and were extremely sensitive to minor changes in boundary conditions such as confinement and stress changes from adjacent excavations. The progressive failure process

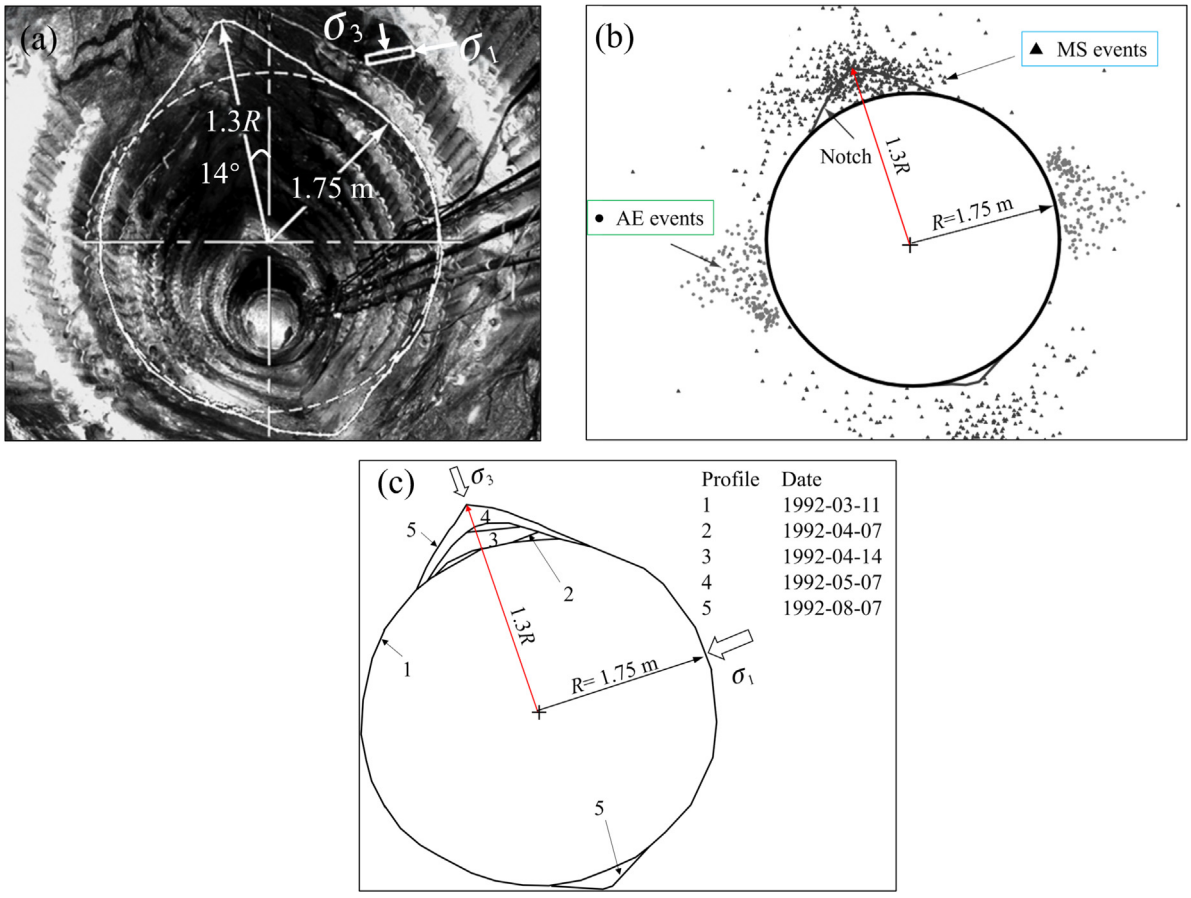

Fig. 11. Field monitoring and observation of the URL. (a) Photograph of the URL test tunnel (Martin, 1997; Reproduced with permission, courtesy of Canadian Science Publishing), (b) indicative locations of the AE and MS events from the URL test tunnel (Cai et al., 2001), and (c) the URL test tunnel and progressive development of the notch geometry (Martin, 1997).

included initiation, dilation, slabbing, spalling, and stabilization. A typical slab generated during the process is shown in Fig. 10(c). The sequence of acoustic emission (AE) and microseism (MS) events leading to failure (Fig. 11(b) and (c)) was similar to that observed in laboratory compression tests on rock samples containing a circular hole.

The URL test tunnel, as a classic engineering case, has been extensively studied by many researchers. Vazaios et al. (2019) used the traditional FDEM model to simulate the fracture process of the surrounding rock during excavation. The simulation results of the high damage zone (HDZ) fracture characteristics and their extent agree well with those of field monitoring, but the ability of the traditional FDEM model to reflect the slabbing and spalling mechanism remains unclear (Fig. 12(a)). The virtual block modeling technique used in this study improves the traditional FDEM model, and the simulation results reveal that tensile fractures occur in the surrounding rock, with exterior rock blocks being ejected as rock slabs.

By applying geostress, the tunnel model reaches the final stress equilibrium state, and tunnel excavation is completed under quasi-static conditions. As shown in Fig. 12(b), the stress contour shows two V-shaped notches, with the HDZ depth being greater at the top than at the bottom. The HDZ depth in the traditional FDEM model is approximately 2.20 m, which is 1.26 times the tunnel radius. In the dsbVBM, the HDZ depth is approximately 2.24 m, which is 1.28 times the tunnel radius. Field observations indicate that the HDZ depth is approximately 1.3 times the tunnel

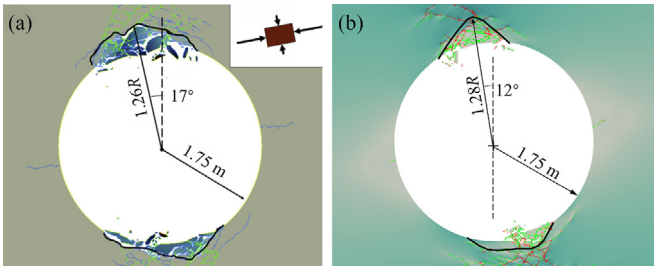

Fig. 12. Comparison between the simulation and field observations. (a) Damage profile from the FDEM model (highlighted in black) after the completion of the numerical analysis (Vazaios et al., 2019; Reproduced with permission, courtesy of Canadian Science Publishing), and (b) damage profile from the FDEM-VBM (highlighted in black) after the completion of the numerical analysis.

radius, and the simulation results agree well with the field observations, indicating the practicality of the dsbVBM.

Through block fracture mode analysis (Fig. 13), inter-block tensile cracks first initiate. The extension of inter-block cracks induces intra-block tensile cracks. The expansion of intra-block cracks leads to far-field inter-block cracks. The inter-block and intra-block cracks connect with each other, forming macroscopic splitting surfaces. The depth at which macroscopic fractures develop within a rock mass depends on the geostress magnitude and rock mass strength. As the distance from the excavation boundary increases, the damage and fracture processes are locally constrained, ultimately leading to the self-stabilization of a V-shaped notch. The VBM can efficiently and accurately predict rock strength and fracture characteristics under laboratory and field conditions.

When simulating the confining pressure effect on the fracture mechanism of deep surrounding rock, especially in terms of the shapes of fractured rock slabs and rock blocks, the traditional FDEM model shows obvious limitations because triangular elements tend to mobilize slip. For unbreakable polygonal block models (Fig. 14(a)), the boundaries of blocks restrict their movement, and additional block roughness limits block sliding, creating rough fracture paths, intensifying tensile fractures and suppressing shear slip. For triangular block models (Fig. 14(b)), these blocks promote shear slip but struggle to activate tensile failure. Specifically, these models have difficulty comprehensively representing the tensile, shear, and mixed fracture processes in hard rock masses. The VBM (Fig. 14(c)) allows fractures to occur between or within blocks, enabling the activation of tensile fractures under low confining pressure conditions, whereas at medium to high confining pressures, it enhances the compressive interaction between blocks to simulate block crushing and block rotation caused by shear sliding.

5.2 Comparison verification with the CJPL-II site

During the construction of the CJPL-II project, the spalling phenomenon is particularly typical. The on-site excavation conditions are shown in Fig. 15. The traditional FDEM model is compared with the dsbVBM. The traditional model cannot sufficiently simulate the tensile mechanism of spalling (Fig. 16(a)), but the VBM improves upon this aspect. The simulation results reveal considerable rock slabs on the left and right sidewalls. Tensile splitting under low confining pressure, mixed tensile and shear fracturing under medium confining pressure, and shear fracture induced by high confining pressure are reflected in the numerical results (Fig. 16(b)).

When the VBM reaches the final stress equilibrium state after excavation is complete, the element node coordinates, crack locations and detached rock masses indicate that the depths of the EDZ and spalling zone at the southern spandrel are 3.29 and 1.33 m, respectively, and those at the north sidewall are 3.06 and 1.26 m, respectively (Fig. 16 (b)). Furthermore, the simulated EDZ profile and rock spalling characteristics are relatively consistent with the field observations (Fig. 16(c) and (d)). Compared with the field observations, the EDZ depth of the southern spandrel is similar to that (3.3 m) observed from digital borehole camera images (Fig. 17). According to the freshness of the joint traces (Fig. 17(b)) on the boreholes, almost all joints are induced by the excavation, indicating that the surrounding rock is very intact before excavation. The fracture opening process gradually decreases with increasing depth (Fig. 17(c)). These findings verify the effectiveness of the VBM in capturing brittle failure, especially rock spalling. The EDZ degree has been successfully simulated via other numerical methods, but the dynamic and morphological characteristics of the spalling rock slabs in the surrounding rock notches cannot be captured or quan-

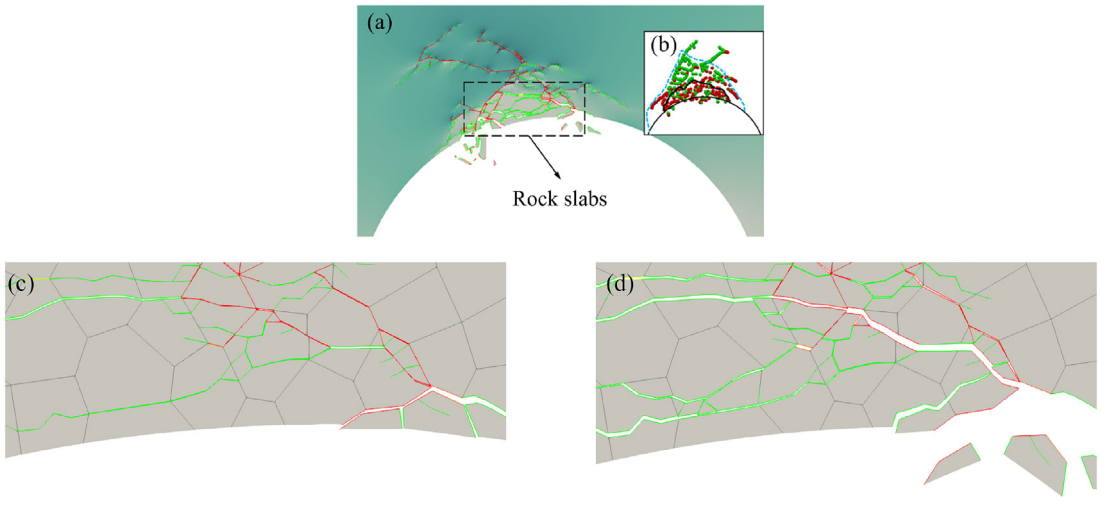

Fig. 13. Typical slab of rock detached from the FDEM-VBM of the URL during the progressive failure process. (a) Overall view of the simulation results, (b) on-site MS data; the red and green points represent tension and shear cracks, respectively, and (c)–(d) partial enlarged views during the simulation.

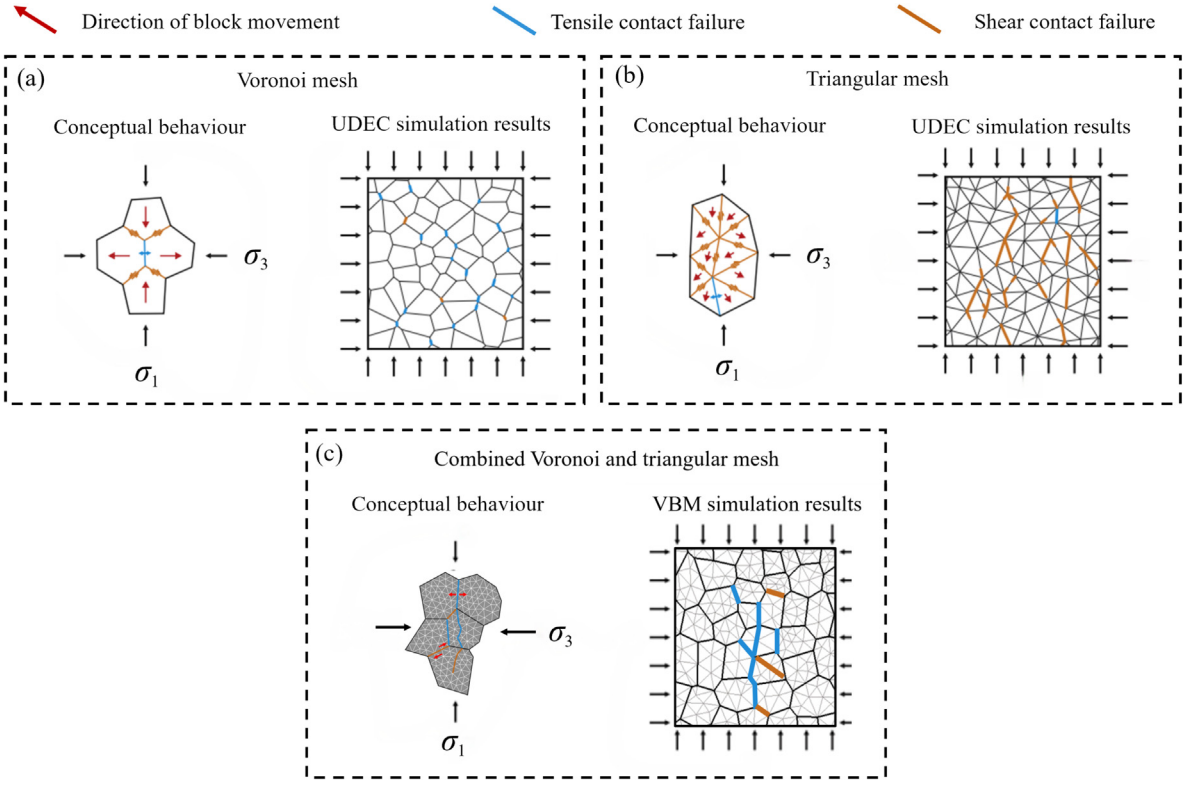

Fig. 14. Comparison of fracture mechanisms for different numerical models. (a) Traditional UDEC model, (b) UDEC-Trigon or traditional FDEM models, and (c) FDEM-VBM.

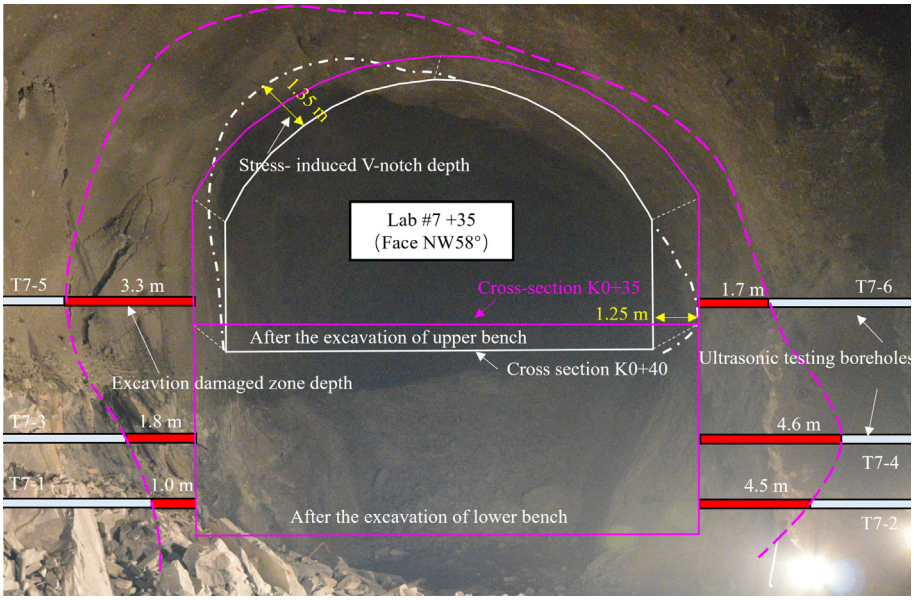

Fig. 15. Field monitoring and observations of the CJPL-II Lab #7 site.

tified. First, the spalling appeared on the sidewalls. As the excavation proceeded, the rock slabs and blocks began to fall, the EDZ further developed into the interior rock mass, the rock bulged outward, the EDZ further expanded, and the rock slabs fell off layer by layer (Fig. 18). Finally, cracks fully penetrated the superficial surrounding rock, many macroscopic fracture surfaces formed, and an EDZ was formed.

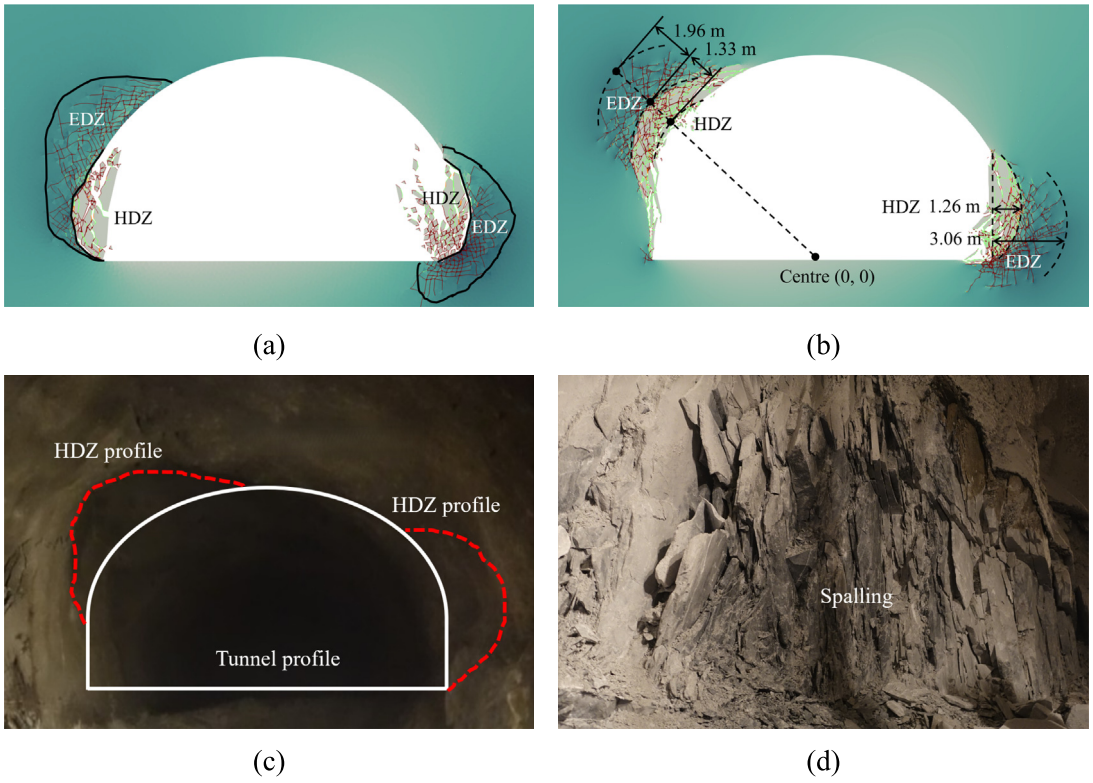

Fig. 16. Comparison of the spalling locations, fracture characteristics, and EDZs of Lab #7 after excavation of the upper bench. (a) EDZ depth simulated via the FDEM-VBM (the green and red segments represent tensile and shear cracks, respectively), (b) EDZ depth simulated via the FDEM, (c) profile of the excavation damage zone, and (d) spalling characteristics of the sidewalls.

To analyze the rock slab thickness, Python was used for image processing of the surrounding rock failure, and it was combined with the Otsu method for optimal thresholding. In the adaptive threshold determination method, the algorithm assumes that image pixels can be divided into background components and objects according to a threshold. The optimal threshold is then calculated to distinguish these two types of pixels, maximize their separation distance, and obtain the minimum bounding rectangle for all irregular rock slabs.

The calculation of the minimum bounding rectangle in Python is based on the concepts of a convex hull and a minimum area rectangle. The convex hull is the smallest convex polygon that contains a set of points that can be used to approximate the shape of an area. The minimum area rectangle is the smallest rectangle that can completely enclose an area, with parallel or perpendicular edges to the contour edges. The minimum bounding rectangle can be obtained by rotating the convex hull. The area of the rotated rectangle is the smallest. The actual dimensions of the minimum bounding rectangle are calculated based on the image pixels, image height, and model coordinate reference system (Fig. 19(a)). Compared with the limited field rock slab data (Fig. 19(b)), the maximum, minimum, and average thickness values of the rock slabs closely match. The characteristics of the field rock slabs are shown in Fig. 20.

6 Discussion

The VBM is derived from the microscopic grain-based model, but the difference is that the rock mass is characterized using breakable Voronoi blocks. These blocks are the potential fracture and energy dissipation paths of the rock mass. The model represents a strain energy dissipation structure and describes the difference in energy consumption of random fracture paths. In actual engineering projects, the fracture paths of intact rock masses tend to be the paths with less energy consumption.

Although the analysis based on the 2D VBM is positive under the plane strain condition, the actual underground engineering structure is usually complex, and the VBM needs to be extended to 3D. A 3D block has true degrees of freedom in motion, including 3D translation and rotation. The 3D model can be used to study more complex geometries and triaxial stress states. Moreover, the deep rock mass structure is usually extremely complex, and the failure characteristics of fractured rock masses are

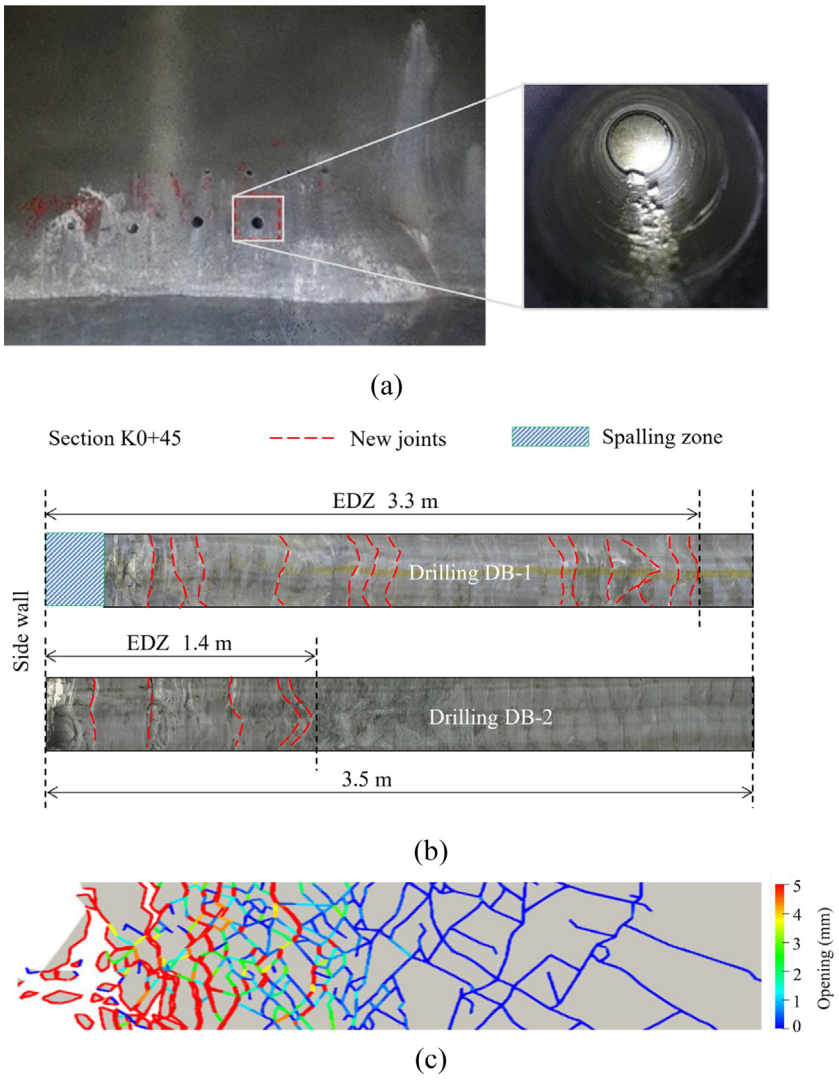

Fig. 17. Field monitoring data. (a) Boreholes and nearly parallel cracks in the boreholes (Feng et al., 2018c), (b) digital borehole camera images of the surrounding rock mass of the CJPL-II Lab #7 site (DB-1 in the southern spandrel and DB-2 in the northern sidewall) (Xu et al., 2022), and (c) simulated apertures of cracks in the left arch shoulder.

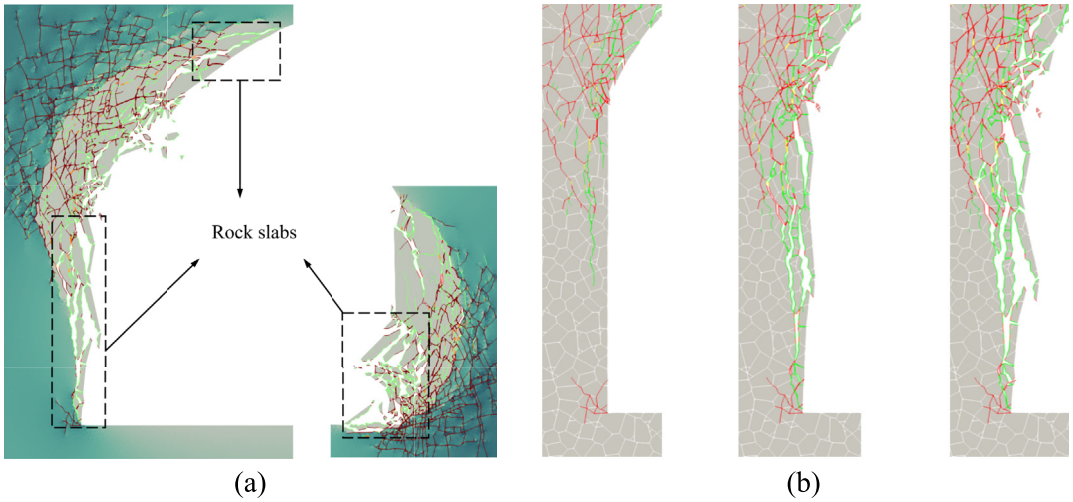

Fig. 18. Excavation damage characteristics of the CJPL-II Lab #7 site. (a) Typical rock slabs detached from the VBM during excavation, and (b) spalling process in the left sidewall.

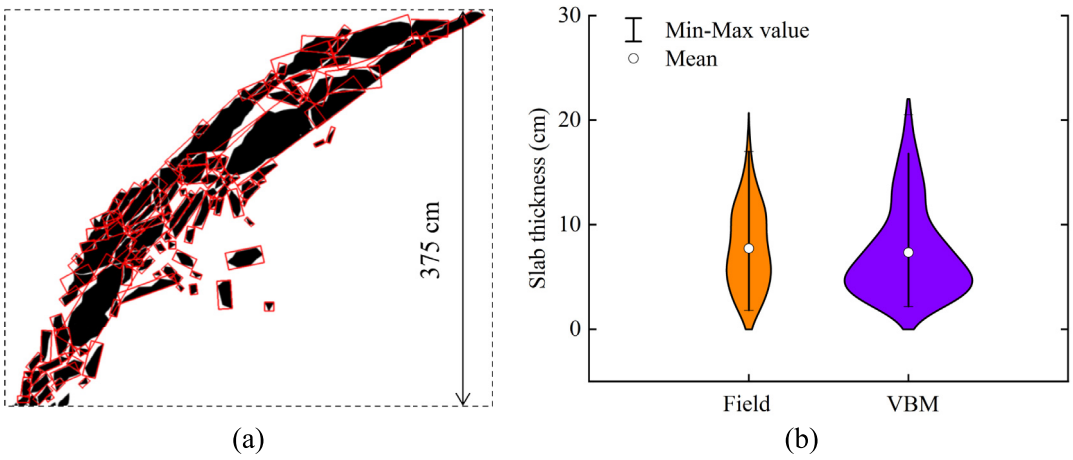

Fig. 19. Identification of slab thickness. (a) Left spandrel, and (b) comparison of the slab thickness between the field data (Feng et al., 2018b) and the numerical results.

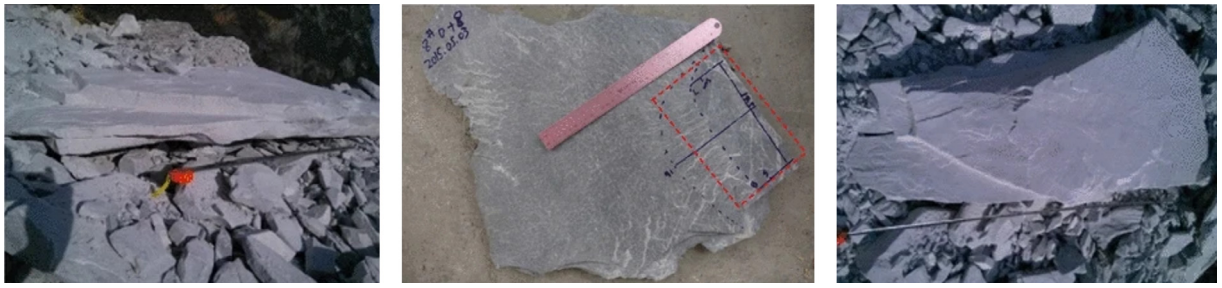

Fig. 20. Shell-shaped and feather-shaped concentric fracture surfaces and combined fracture surfaces (Feng et al., 2018b).

completely different from those of intact rock masses. Therefore, the model needs to be expanded to consider the discrete fracture network (DFN).

7 Conclusions

In this study, an upscaling hierarchical grain-based approach is proposed to simulate the fracture of the EDZ in intact rock masses and assess the thickness of spalling rock slabs. The main conclusions are as follows:

(1) The typical surrounding rock damage phenomenon demonstrates that the dominant surrounding rock damage mechanism is stress-induced extensional cracking, which results in the formation of many spalling rock slabs. However, after the formation of parallel slabs, the subsequent loading of axial strain causes the slabs to be prone to buckling or bulging due to the geometric mismatch between them. These behaviors are more prominent in local fractured rock masses, during which the shear damage between the slabs or blocks is also gradually highlighted.

(2) Excavation of deeply buried tunnels typically results in strain-induced fractures. During excavation and unloading, the surrounding rock releases stored elastic energy, which is reflected in the form of tensile stress waves at the excavation boundary. When the tensile stress exceeds the rock tensile strength, fracture surfaces form nearly parallel to the excavation boundary, resulting in spalling failure. This work confirms the practicality of the dsbVBM for simulating the evolution of the EDZ of hard rock masses in deeply buried tunnels. The simulation reproduces the field EDZ phenomena and is comparable to the actual EDZ observations from the Canadian URL test tunnel and the CJPL-II Lab #7 sites.

(3) The proposed parameter scaling method, which considers the fracture morphology of the rock mass and computational efficiency, can be used to rapidly calibrate engineering-scale model parameters. Theoretical and numerical empirical formulas for determining the block size are provided. The numerical results reveal excavation damage characteristics. In particular, the VBM clearly captures the fracturing processes of tensile splitting under low confining pressure, mixed fracture under moderate confining pressure, and shear fracture under high confining pressure. Moreover, the Otsu method can be used to evaluate the thicknesses of the spalling rock slabs effectively.

Data availability

The data that support the findings of this study are available from the corresponding author upon reasonable request.

CRediT authorship contribution statement

Shili Qiu: Writing – review & editing, Supervision, Software, Project administration, Funding acquisition. **Shirui Zhang:** Writing – original draft, Visualization, Validation, Software, Methodology, Investigation, Formal analysis, Data curation, Conceptualization. **Quan Jiang:** Writing – review & editing, Supervision, Project administration, Funding acquisition. **Yuheng Fang:** Investigation. **Ping Li:** Investigation. **Shaojun Li:** Project administration. **Yaxun Xiao:** Data curation. **Dingping Xu:** Data curation.

Declaration of competing interest

The authors declare that they have no known competing financial interests or personal relationships that could have appeared to influence the work reported in this paper.

Acknowledgement

The authors acknowledge the financial support received from the National Natural Science Foundation of China (Grant Nos. 52325905 and 42377172).

References

Abdelaziz, A., Zhao, Q., & Grasselli, G. (2018). Grain based modelling of rocks using the combined finite-discrete element method. *Computers and Geotechnics, 103*, 73–81.

Cai, M., Kaiser, P. K., & Martin, C. D. (2001). Quantification of rock mass damage in underground excavations from microseismic event monitoring. *International Journal of Rock Mechanics and Mining Sciences, 38*(8), 1135–1145.

Curran, J. H., Hammah, R. E., & Yacoub, T. E. (2003). A two-dimensional approach for designing tunnel support in weak rock. *Proceedings of the 56th Canadian Geotechnology Conference*. .

Dadashzadeh, N. (2020). *Reliability of Stress Induced Damage Predictions in Hard Rocks with Continuum and Discontinuum Numerical Modelling Approaches* [Doctoral dissertation, Queen's University].

Diederichs, M. S. (2003). Manuel rocha medal recipient rock fracture and collapse under low confinement conditions. *Rock Mechanics and Rock Engineering, 36*(5), 339–381.

Diederichs, M. S. (2007). The 2003 Canadian geotechnical colloquium: Mechanistic interpretation and practical application of damage and spalling prediction criteria for deep tunnelling. *Canadian Geotechnical Journal, 44*(9), 1082–1116.

Evans, R. H., & Marathe, M. S. (1968). Microcracking and stress-strain curves for concrete in tension. *Matériaux et Constructions, 1*(1), 61–64.

Farahmand, K., & Diederichs, M. S. (2021). Calibration of coupled hydro-mechanical properties of grain-based model for simulating fracture process and associated pore pressure evolution in excavation damage zone around deep tunnels. *Journal of Rock Mechanics and Geotechnical Engineering, 13*(1), 60–83.

Farahmand, K., Vazaios, I., Diederichs, M. S., & Vlachopoulos, N. (2018). Investigating the scale-dependency of the geometrical and mechanical properties of a moderately jointed rock using a synthetic rock mass (SRM) approach. *Computers and Geotechnics, 95*, 162–179.

Feng, X. T., Guo, H. S., Yang, C. X., & Li, S. J. (2018a). In situ observation and evaluation of zonal disintegration affected by existing fractures in deep hard rock tunneling. *Engineering Geology, 242*, 1–11.

Feng, X. T., Yao, Z. B., Li, S. J., Wu, S. Y., Yang, C. X., Guo, H. S., & Zhong, S. (2018b). In situ observation of hard surrounding rock displacement at 2400-m-deep tunnels. *Rock Mechanics and Rock Engineering, 51*(3), 873–892.

Feng, X., Xu, H., Qiu, S., Li, S., Yang, C., Guo, H., Cheng, Y., & Gao, Y. (2018c). In situ observation of rock spalling in the deep tunnels of the China Jinping Underground Laboratory (2400 m depth). *Rock Mechanics and Rock Engineering, 51*(4), 1193–1213.

Feng, X., Zhang, C., Qiu, S., Zhou, H., Jiang, Q., & Li, S. (2016). Dynamic design method for deep hard rock tunnels and its application. *Journal of Rock Mechanics and Geotechnical Engineering, 8*(4), 443–461.

Gao, F., Kaiser, P. K., Stead, D., Eberhardt, E., & Elmo, D. (2019). Numerical simulation of strainbursts using a novel initiation method. *Computers and Geotechnics, 106*, 117–127.

Gao, F., Stead, D., & Elmo, D. (2016). Numerical simulation of microstructure of brittle rock using a grain-breakable distinct element grain-based model. *Computers and Geotechnics, 78*, 203–217.

Geomechanica Inc. (2021). *Irazu 2D geomechanical simulation software, version 4.0*.

Geuzaine, C., & Remacle, J.-F. (2009). Gmsh: A 3-D finite element mesh generator with built-in pre- and post-processing facilities. *International Journal for Numerical Methods in Engineering, 79*(11), 1309–1331.

Hajiabdolmajid, V., Kaiser, P. K., & Martin, C. D. (2002). Modelling brittle failure of rock. *International Journal of Rock Mechanics and Mining Sciences, 39*(6), 731–741.

Hu, X., Gong, X., Xie, N., Zhu, Q., Guo, P., Hu, H., & Ma, J. (2022). Modeling crack propagation in heterogeneous granite using grain-based phase field method. *Theoretical and Applied Fracture Mechanics, 117*, 103203.

Hu, X., Hu, H., Xie, N., Huang, Y., Guo, P., & Gong, X. (2023). The effect of grain size heterogeneity on mechanical and microcracking behavior of pre-heated lac du bonnet granite using a grain-based model. *Rock Mechanics and Rock Engineering, 56*(8), 5923–5954.

Hu, X., Xie, N., Zhu, Q., Chen, L., & Li, P. (2020). Modeling damage evolution in heterogeneous Granite using digital image-based grain-based model. *Rock Mechanics and Rock Engineering, 53*(11), 4925–4945.

Jing, L., & Hudson, J. A. (2002). Numerical methods in rock mechanics. *International Journal of Rock Mechanics and Mining Sciences, 39*(4), 409–427.

Kim, K., Rutqvist, J., Nakagawa, S., & Birkholzer, J. (2017). TOUGH–RBSN simulator for hydraulic fracture propagation within fractured media: Model validations against laboratory experiments. *Computers & Geosciences, 108*, 72–85.

Li, X., Li, H., Liu, L., Liu, Y., Ju, M., & Zhao, J. (2020). Investigating the crack initiation and propagation mechanism in brittle rocks using grain-based finite-discrete element method. *International Journal of Rock Mechanics and Mining Sciences, 127*, 104219.

Lisjak, A., Mahabadi, O. K., He, L., Tatone, B. S. A., Kaifosh, P., Haque, S. A., & Grasselli, G. (2018). Acceleration of a 2D/3D finite-discrete element code for geomechanical simulations using general purpose GPU computing. *Computers and Geotechnics, 100*, 84–96.

Martin, C. D. (1997). Seventeenth Canadian geotechnical colloquium: The effect of cohesion loss and stress path on brittle rock strength. *Canadian Geotechnical Journal, 34*(5), 698–725.

Martin, C. D., Kaiser, P. K., & McCreath, D. R. (1999). Hoek-Brown parameters for predicting the depth of brittle failure around tunnels. *Canadian Geotechnical Journal, 36*(1), 136–151.

Munjiza, A., & Andrews, K. R. F. (2000). Penalty function method for combined finite-discrete element systems comprising large number of separate bodies. *International Journal for Numerical Methods in Engineering, 49*(11), 1377–1396.

Munjiza, A., Owen, D. R. J., & Bicanic, N. (1995). A combined finite-discrete element method in transient dynamics of fracturing solids. *Engineering Computations, 12*(2), 145–174.

Peng, J., Wong, L. N. Y., Teh, C. I., & Li, Z. (2018). Modeling micro-cracking behavior of Bukit Timah granite using grain-based model. *Rock Mechanics and Rock Engineering, 51*(1), 135–154.

Perras, M. A., & Diederichs, M. S. (2014). A review of the tensile strength of rock: Concepts and testing. *Geotechnical and Geological Engineering, 32*(2), 525–546.

Qiu, S., Feng, X., Zhang, C., & Xiang, T. (2014). Estimation of rockburst wall-rock velocity invoked by slab flexure sources in deep tunnels. *Canadian Geotechnical Journal, 51*(5), 520–539.

Quey, R., Dawson, P. R., & Barbe, F. (2011). Large-scale 3D random polycrystals for the finite element method: Generation, meshing and remeshing. *Computer Methods in Applied Mechanics and Engineering, 200*(17–20), 1729–1745.

Read, R. S. (2004). 20 years of excavation response studies at AECL's underground research laboratory. *International Journal of Rock Mechanics and Mining Sciences, 41*(8), 1251–1275.

Ren, H., Zhuang, X., Bie, Y., Rabczuk, T., & Zhu, H. (2025). Dual-horizon peridynamics-based variational damage modeling for complex dynamic fractures. *Theoretical and Applied Fracture Mechanics, 138*, 104974.

Ren, H., Zhuang, X., Cai, Y., & Rabczuk, T. (2016). Dual-horizon peridynamics. *International Journal for Numerical Methods in Engineering, 108*(12), 1451–1476.

Ren, H., Zhuang, X., & Rabczuk, T. (2020). A higher order nonlocal operator method for solving partial differential equations. *Computer Methods in Applied Mechanics and Engineering, 367*, 113132.

Ren, H., Zhuang, X., Zhu, H., & Rabczuk, T. (2024). Variational damage model: A novel consistent approach to fracture. *Computers & Structures, 305*, 107518.

Sinha, S., & Walton, G. (2018). A progressive S-shaped yield criterion and its application to rock pillar behavior. *International Journal of Rock Mechanics and Mining Sciences, 105*, 98–109.

Sinha, S., & Walton, G. (2021). Investigation of pillar damage mechanisms and rock-support interaction using Bonded Block Models. *International Journal of Rock Mechanics and Mining Sciences, 138*, 104652.

Tatone, B. S. A., & Grasselli, G. (2015). A calibration procedure for two-dimensional laboratory-scale hybrid finite–discrete element simulations. *International Journal of Rock Mechanics and Mining Sciences, 75*, 56–72.

Vazaios, I., Vlachopoulos, N., & Diederichs, M. S. (2019). Mechanical analysis and interpretation of excavation damage zone formation around deep tunnels within massive rock masses using hybrid finite–discrete element approach: Case of Atomic Energy of Canada Limited (AECL) Underground Research Laboratory (URL) test tunnel. *Canadian Geotechnical Journal, 56*(1), 35–59.

Vlachopoulos, N., & Diederichs, M. S. (2014). Appropriate uses and practical limitations of 2D numerical analysis of tunnels and tunnel support response. *Geotechnical and Geological Engineering, 32*(2), 469–488.

Walton, G., Diederichs, M. S., Alejano, L. R., & Arzúa, J. (2014). Verification of a laboratory-based dilation model for in situ conditions using continuum models. *Journal of Rock Mechanics and Geotechnical Engineering, 6*(6), 522–534.

Wang, X., & Cai, M. (2018). Modeling of brittle rock failure considering inter- and intra-grain contact failures. *Computers and Geotechnics, 101*, 224–244.

Xu, D., Huang, X., Li, S., Xu, H., Qiu, S., Zheng, H., & Jiang, Q. (2022). Predicting the excavation damaged zone within brittle surrounding rock masses of deep underground caverns using a comprehensive approach integrating in situ measurements and numerical analysis. *Geoscience Frontiers, 13*(2), 101273.

Zhang, S., Qiu, S., Jiang, Q., Kou, Y., Jia, L., & Wang, H. (2024a). Mechanical and cracking behavior of granite specimens containing various inclusions. *Computers and Geotechnics, 167*, 106122.

Zhang, S., Qiu, S., Jiang, Q., Yan, C., Zhou, L., & Li, X. (2024b). Modeling damage evolution in granite under temperature using a thermo-mechanical grain-based FDEM model. *Computers and Geotechnics, 169*, 106198.

Zhong, S., Jiang, Q., Feng, X., Liu, J., Li, S., Qiu, S., & Wu, S. (2018). A case of in-situ stress measurement in Chinese Jinping underground laboratory. *Rock and Soil Mechanics, 39*(1), 356–366.